

Article

# Sediment Transport Processes during Barrier Island Inundation under Variations in Cross-Shore Geometry and Hydrodynamic Forcing

Anita Engelstad <sup>\*</sup>, Gerben Ruessink , Piet Hoekstra  and Maarten van der Vegt Department of Physical Geography, Faculty of Geosciences, Utrecht University,  
3508 TC Utrecht, The Netherlands

\* Correspondence: A.C.Engelstad@uu.nl or anitaengel@gmx.net

Received: 5 May 2019; Accepted: 3 July 2019; Published: 8 July 2019



**Abstract:** Inundation of barrier islands can cause severe morphological changes, from the break-up of islands to sediment accretion. The response will depend on island geometry and hydrodynamic forcing. To explore this dependence, the non-hydrostatic wave model SWASH was used to investigate the relative importance of bedload transport processes, such as transport by mean flow, short- (0.05–1 Hz) and infragravity (0.005–0.05 Hz) waves during barrier island inundation for different island configurations and hydrodynamic conditions. The boundary conditions for the model are based on field observations on a Dutch barrier island. Model results indicate that waves dominate the sediment transport processes from outer surfzone until landwards of the island crest, either by transporting sediment directly or by providing sediment stirring for the mean flow transport. Transport by short waves was continuously landwards directed, while infragravity wave and mean flow transport was seaward or landward directed. Landward of the crest, sediment transport was mostly dominated by the mean flow. It was forced by the water level gradient, which determined the mean flow transport direction and magnitude in the inner surfzone and on the island top. Simulations suggest that short wave and mean flow transport are generally larger on steeper slopes, since wave energy dissipation is less and mean flow velocities are higher. The slope of the island top and the width of the island foremost affect the mean flow transport, while variations in inundation depth will additionally affect transport by short-wave acceleration skewness.

**Keywords:** sediment transport; barrier island inundation; numerical modeling (SWASH)

## 1. Introduction

The response of barrier islands to overwash (water overtops the beach- or dune crest without directly returning to the sea [1]) and inundation (the area is continuously submerged [2]) differs strongly between islands. It can include erosion such as shoreline retreat and breaching [1,3], the landward migration of islands, also termed “roll-over” [1], and sediment accretion such as gains in subaerial areas [4]. A crucial component that determines the morphological change of barrier islands is the island geometry. Low profile, narrow islands can be found primarily in wave-dominated, microtidal systems (tidal range < 2 m) such as in the Gulf of Mexico (USA). These barriers have a high risk of erosion, roll-over and break-up, since the barrier response to overwash and inundation depends at least partly on dune-elevation and barrier width in addition to hydrodynamic forcing (e.g., [2,5,6]). Generally, barrier island width appears to be a factor that determines subaerial deposition or the landward migration of barrier islands [6]. The wide and high barrier islands in mixed energy systems (tidal range 2–4 m), such as in the Wadden Sea, which is fronting Denmark, Germany, and the Netherlands, have the potential to accrete sediment [7]. Observations in the Netherlands on part of a barrier island with a

width of  $\sim 1.3$  km, which is subjected to winter cold fronts and regular inundation, suggested that the subaerial part of the study area accreted sediment [7,8]. Additional observations of hydrodynamics and suspended sediment concentrations at the beach crest related this to landward transport. From these observations, Engelstad et al. [7] defined two transport regimes for the Dutch barrier island. If flow velocities were high ( $>0.5$  m/s), which was frequently the case before high tide when water levels at the island crest exceeded the water levels in the basin, the transport was dominated by the flow. When flow velocities were low, the sediment suspension and transport was episodic on an infragravity time-scale. It is, however, unknown what the sediment transport processes were seaward of the crest or how stirring and transport by waves and currents would differ on a steeper bed slope. Additionally, the question remained if the observed suspension on infragravity (IG) time scales was primarily caused by the IG waves themselves, or by larger short waves riding the crests of IG waves. Sediment transport can also be influenced by the gradient in water levels between ocean and back barrier basin (lagoon). It has been shown to greatly affect magnitude and direction of sediment transport on barrier islands in the Gulf of Mexico and in the Wadden Sea [7,9–12].

The relative contribution of IG waves, short waves and mean flow to the net sediment transport will at least partly depend on the bed slope steepness, since it affects the wave shape and energy dissipation [13,14]. For a closed beach system, De Bakker et al. [15] showed that IG sediment transport and direction is dependent on the beach slope steepness. In the inner surf zone, IG transport was onshore directed for a steeper slope (1:35) where it contributed less than 20% to the total cross-shore sand flux, and seaward directed for a gentle slope (1:80) with a contribution of up to 60%. Furthermore, studies suggest that the wave field on steep slopes close to shore is dominated by short wave (0.05–1 Hz) motion, while on gentle slopes IG waves are dominant (e.g., [16–18]). However, these processes might differ in an open boundary system as during inundation.

In the last several years, design criteria for barrier island restoration have been developed. Considerations include the island width, height and the potential for the consolidation of sediment, as well as the storm forcing [6,19,20]. For example, on Assateague Island, Maryland, USA, island elevation and stability were increased by cutting notches through the foredunes [20], which allowed overwash to deposit sand in the interior of the island. In the Netherlands, efforts to mitigate the effects of the expected sea level rise are on the way. Large parts of the barrier coastline are now protected by artificial sand drift dikes, which prevent landward migration and the accumulation of sediment landwards of the dikes. Hence, the partial reopening of dunes and dikes is considered, to allow natural dynamics such as overwash and inundation. A better understanding of the effect that island geometries and hydrodynamic forcing have on sediment transport will optimize design criteria for restoration efforts.

The goal of this study is to improve our knowledge of sediment stirring and transport processes from the outer surfzone to the back barrier basin during barrier island inundation and the effect that island slopes and hydrodynamic forcing have on these processes. For this, the numerical model SWASH (Simulating WAVes till SHore) [21] was used under variations in island geometries and hydrodynamic forcing conditions. SWASH is a phase resolving, nonhydrostatic wave-model, which has been shown to successfully hindcast field and laboratory conditions [18,22–25]. The boundary conditions, such as wave heights and water levels, were based on observations [7] to allow insight into Wadden Sea processes, while modifications represent extremes and can be also applied to other systems. SWASH is described in Section 2, and a validation of the model with observations [7] can be found in Appendix A. The sediment transport model, data analysis and experiments will also be introduced in Section 2. Results for a comparison of sediment transport mechanism between a 1:30 and a 1:120 slope will be shown in Section 3, in addition to results for changes in the hydrodynamic forcing. The implications of our results will be discussed in Section 4, and we will summarize the findings in Section 5.

## 2. Methods

### 2.1. Model Description

In order to accurately model the hydrodynamics during inundation and to include wave-shape effects in the investigation of sediment transport processes, the model approach was two-fold. The phase resolving, nonhydrostatic wave-model SWASH [21] was used to simulate the hydrodynamics (see Section 2.1.1), since field observations showed that IG and short waves were highly nonlinear and broke on the submerged island during inundation [8]. Additionally, IG bores propagated onshore and high sediment suspension was observed on IG time-scales, highlighting the possible importance of IG waves in sediment suspension and transport [7]. SWASH has been shown to accurately hindcast hydrodynamic bulk properties, such as wave heights and periods, and detailed nonlinear interactions in the laboratory [18,22,23] as well as being able to represent conditions found in the field [24,25]. For this study, the boundary conditions are primarily based on field observations collected in 2017 [7] to give insight into sediment transport processes during the inundation of barrier islands in the Wadden Sea region, and how these processes change with a change in forcing and island geometry. This in turn reflects also on conditions in other systems.

2D simulations in SWASH are very time-consuming, and since we want to use the model in an exploratory way (by exploring the differences in island geometry and hydrodynamic forcing on wave and current stirring and transport), we used SWASH in 1D mode. While this allowed us to run comparisons in a timely manner, it had the drawback of leading to an overestimation in IG wave heights of roughly 100% when compared to observations (see Appendix A). This overestimation of IG wave energy by SWASH, also observed by e.g., De Bakker et al. [14], Fiedler et al. [25], and Rijnsdorp et al. [26], is caused by the fact that directional spreading cannot be included in 1D mode, leading to an overestimation for waves in the low-frequency range [27]. While IG energy will be overestimated for all experiments, the effect of island geometry and hydrodynamic forcing on IG wave stirring and transport can still be estimated. We will, however, avoid comparing transport processes, such as IG and short wave transport, with each other in an absolute sense.

Next, in the model approach, an energetics based bedload sediment transport model [28,29] was used (described in Section 2.1.2) to estimate stirring and transport by mean flow and waves. To simplify the analysis, we assume that wave and current processes have the same (relative) importance for suspended load as for bedload processes, since both are a function of flow velocity (to the power of 3 for bed load and to the power of 4 for suspended load, Bailard [29]), and so here we only consider the time-averaged cross-shore bedload transport and ignore suspended-load and gravity-driven transport. This then also ignores any effects of phase lags between the suspended sediment concentrations and the velocity field. The effect of wave asymmetry was added by using the formulation of Drake and Calantoni [30] and Hoefel and Elgar [31] which estimates the effect of acceleration skewness through the bedload.

#### 2.1.1. Hydrodynamic Model—SWASH

SWASH is based on the nonlinear shallow water equations, which describe the conservation of mass and the momentum balance, and accounts for non-hydrostatic pressure. For a full model description, see Zijlema et al. [21]. Since in this study SWASH is used in the cross-shore (unidirectional) mode, the governing equations are

$$\frac{\partial u}{\partial t} + \frac{\partial u^2}{\partial x} + \frac{\partial wu}{\partial z} = -\frac{1}{\rho} \frac{\partial (p_h + p_{nh})}{\partial x} + \frac{\partial \tau_{xz}}{\partial z} + \frac{\partial \tau_{xx}}{\partial x}, \quad (1)$$

$$\frac{\partial w}{\partial t} + \frac{\partial uw}{\partial x} + \frac{\partial w^2}{\partial z} = -\frac{1}{\rho} \frac{\partial (p_{nh})}{\partial z} + \frac{\partial \tau_{zz}}{\partial z} + \frac{\partial \tau_{zx}}{\partial x}, \quad (2)$$

$$\frac{\partial u}{\partial x} + \frac{\partial w}{\partial z} = 0, \tag{3}$$

where  $u(x, z, t)$  and  $w(x, z, t)$  are the horizontal and vertical velocities, respectively.  $\rho$  is the fluid density,  $p_h$  and  $p_{nh}$  are the hydrostatic and non-hydrostatic pressure contributions and  $\tau$  describes the turbulent stresses. The evolution of the free surface  $\zeta$  is given by

$$\frac{\partial \zeta}{\partial t} + \frac{\partial}{\partial x} \int_{-d}^{\zeta} u dz = 0, \tag{4}$$

where  $z = -d$  indicates the bottom. The bottom friction term  $\tau_b$ , used at the bottom boundary, is based on the quadratic friction law

$$\tau_b = c_f \frac{U|U|}{h}, \tag{5}$$

where  $U$  is the depth averaged velocity and  $h$  is the water depth. The bed friction coefficient,  $c_f$ , is calculated as

$$c_f = \frac{n^2 g}{h^{\frac{1}{3}}}, \tag{6}$$

where  $g$  is acceleration due to gravity. Here, the Manning’s roughness coefficient,  $n$ , was set to its default of 0.019. Vertical mixing was included to increase the stability of the model by setting the vertical viscosity to  $3 \times 10^{-4} \text{ m}^2/\text{s}$ . Horizontal turbulent mixing was ignored. The vertical resolution for the model runs was set to two vertical layers. Therefore, dissipation by wave breaking was captured with the hydrostatic front approximation, HFA, which imposes a hydrostatic pressure distribution at the wave front and initiates wave breaking [32]. The steepness criterion for the rate of surface rise to initiate wave breaking,  $\alpha$ , was set to 0.6 and the criterion for the persistence of wave breaking,  $\beta$ , was set to 0.3 for the experiments (following the recommendations by Smit et al. [32] for two layers), and varied in the model-data comparison (see Appendix A.1). The stability of the computations was assured by setting the time-step, based on the Courant number, to 0.0125 s for all runs. Simulations were run over 2 h to allow for sufficient spin-up time over the large domain (described below), and bulk parameters were averaged over the last hour. At the ocean side, the boundary type was chosen to be weakly reflective, while at the basin side a 500 m sponge layer was used to avoid wave reflection. Further model implementations, the model domain, and the boundary conditions are described in detail in Section 2.2.

### 2.1.2. Sediment Transport Model

We used the modification by Drake and Calantoni [30] of Bailard’s (1981) bed load sediment transport equation for the sediment transport model. The mass sediment bedload transport per unit width and per unit time,  $q$ , is given as

$$q_b = K_b (\langle |u(t)|^2 u(t) \rangle), \tag{7}$$

where the brackets denote time averages and

$$K_b = \frac{\rho_s}{g(\rho_s - \rho_w)} \rho_w c_f \frac{\epsilon_b}{\tan(\phi)}. \tag{8}$$

$\rho_s$  and  $\rho_w$  are the densities of sand and water, respectively, and are here taken as  $2650 \text{ kg/m}^3$  and  $1025 \text{ kg/m}^3$ . The efficiency factor  $\epsilon_b$  is set to 1.03 following Drake and Calantoni [30]. This factor is larger than  $\epsilon_b = 0.135$ , which was used by Thornton et al. [33] and Gallagher et al. [34], and the difference between these factors will be discussed in Section 4.3. The angle of internal friction for sand grains,  $\tan(\phi)$ , is set to 0.63 [33]. While most studies set  $c_f = 0.003$  [30,33,34], we used Equation (6) to account for the effect of varying depths in bathymetry.

The instantaneous cross-shore velocity  $u(t)$  is the sum of mean flow  $\bar{u}$  and oscillating components

$$u(t) = \bar{u} + u_{ig}(t) + u_{short}(t), \tag{9}$$

where  $u_{ig}(t)$  and  $u_{short}(t)$  are the IG (0.005–0.05 Hz) and short wave (0.05–1 Hz) contributions, respectively. The velocity moments in Equation (7) can be expressed as

$$\langle |u|^2 u \rangle = \langle (\bar{u} + u_{ig} + u_{short})^2 (\bar{u} + u_{ig} + u_{short}) \rangle. \tag{10}$$

The expansion of Equation (10) yields

$$\begin{aligned} \langle |u|^2 u \rangle = & \bar{u}^3 (1) + 3\bar{u} \langle u_{ig}^2 \rangle (2) + \langle u_{ig} u_{ig}^2 \rangle (3) \\ & + 3 \langle u_{short} u_{ig}^2 \rangle (4) + 3\bar{u} \langle u_{short}^2 \rangle (5) \\ & + 3 \langle u_{ig} u_{short}^2 \rangle (6) + \langle u_{short} u_{short}^2 \rangle (7), \end{aligned} \tag{11}$$

where we omitted terms that do not contribute to sediment transport such as, for example,  $3 \langle u_{short} \bar{u}^2 \rangle$  (since the mean of the oscillatory motion  $u_{short}$  is zero). The numbers in round brackets given in Equation (11) are given for the following reference. Term (1) on the right side of the equation describes transport and stirring by the mean flow. Terms (2)–(4) represent sediment stirring by infragravity waves and transport by the mean flow (2), IG- (3), and short waves (4). Furthermore, terms (5)–(7) describe transport which is stirred by short waves and, again, transported by the mean flow (5), IG- (6) and short waves (7). In this way, cubed terms for the short and IG waves represent transport by wave skewness. Then,

$$q_{mean} = K_b (\bar{u}^3 + 3\bar{u} \langle u_{ig}^2 \rangle + 3\bar{u} \langle u_{short}^2 \rangle), \tag{12}$$

$$q_{short} = K_b (3 \langle u_{short} u_{ig}^2 \rangle + \langle u_{short}^3 \rangle), \tag{13}$$

$$q_{ig} = K_b (\langle u_{ig}^3 \rangle + 3 \langle u_{ig} u_{short}^2 \rangle), \tag{14}$$

where  $q_{mean}$  is the total bedload transport by the mean flow,  $q_{short}$  is the total bedload transport due to short waves and  $q_{ig}$  is the total bedload transport by IG waves.

The change in wave shape, as described by wave skewness (long elongated troughs and narrow steep wave crests) and wave asymmetry (steep wave fronts), was quantified as

$$Sk = \frac{\langle \eta^3 \rangle}{\langle \eta^2 \rangle^{\frac{3}{2}}}, \tag{15}$$

$$As = \frac{\langle (hil(\eta))^3 \rangle}{\langle \eta^2 \rangle^{\frac{3}{2}}}, \tag{16}$$

where  $Sk$  describes wave skewness and  $As$  wave asymmetry, while  $hil$  is the Hilbert transform. Velocity skewness and asymmetry can be estimated in the same manner, by replacing  $\eta$  with  $u$ . To estimate the effect of short-wave acceleration skewness on sediment transport (IG-wave acceleration skewness is small and therefore ignored here), we used the formulations of Drake and Calantoni [30] and Hoefel and Elgar [31]:

$$q_{shortA} = K_a (a_{spike} - \text{sgn}(a_{spike}) a_{crit}) \text{ for } |a_{spike}| \geq a_{crit} \tag{17}$$

and

$$q_{shortA} = 0 \text{ for } |a_{spike}| < a_{crit}, \tag{18}$$

where the fluid-motion descriptor  $a_{spike}$  [30] is calculated as

$$a_{spike} = \frac{\langle a(t)^3 \rangle}{\langle a(t)^2 \rangle}. \quad (19)$$

$a(t)$  is the magnitude of the instantaneous fluid acceleration,  $sgn(a_{spike})$  is the sign of the acceleration skewness which can be positive or negative, and  $a_{crit}$  is the critical threshold for the transport initiation. Drake and Calantoni [30] found best results for  $K_a = 0.07 \times 10^{-4} \text{ kg s m}^{-2}$  and  $a_{crit} = 1 \text{ m s}^{-2}$  from highly idealized discrete-particle simulations, while for field data Hoefel and Elgar [31] found  $K_a = 0.37 \text{ kg s m}^{-2}$  and  $a_{crit} = 0.2 \text{ m s}^{-2}$ , which are used here. Hoefel and Elgar [31] attributed the difference between their values and those found by Drake and Calantoni [30] to random waves, breaking induced turbulence and variations in grain size shapes and sizes. We will discuss the variability in results caused by variations in  $K_a$  in Section 4.3.

## 2.2. Model Implementations and Experiment Set-Up

In the following, the implementations of the boundary conditions for the model runs and the experiment set-up are described. A model-data comparison was done and can be found in the Appendix. The model-data comparison was made more difficult by our choice of using the 1D version of the model, by local wave generation (which is not included in the model), and by strong alongshore components of the flow. In addition, the offshore wave direction was obliquely incident ( $\theta$  was between 307 and 335 degrees) at the field site which was oriented  $-10$  degrees from true East. However, results showed high model skill and  $r^2$  values for short wave heights, water levels, and flow velocities on the submerged island (observations further seawards were not available). In addition, the model was able to hindcast the water levels variations caused by the tidal cycle and elevated water levels in the Wadden Sea.

### 2.2.1. Field Observations

Field observations were used to validate the SWASH model (see Appendix A for the model-data comparison) and as boundary conditions for the experiments. These observations were collected during several inundation events on the barrier island Schiermonnikoog (Figure 1), Netherlands, during the winter of 2016/2017 (for details on data collection and analysis, see [7]).



**Figure 1.** The barrier island of Schiermonnikoog is located in the North Sea and is separated from the Dutch coast by the Wadden Sea. The field site was located on the eastern tip of the island, indicated in red.

The field area was located on the island tail which is approximately alongshore uniform and low-lying. The height of the island crest, which was the highest point in the profile (Figure 2a), increased from ~1.7 m to 1.8 m above mean sea level (MSL) during the observational period. The beach slope between 0 m MSL and the island crest changed from 1:80 (initial) to 1:160 (final) as the island crest transitioned landward during the field campaign. Data were collected by an instrument transect that was positioned approximately cross-shore from the North Sea side to the backbarrier basin (Wadden Sea) (Figure 2a).

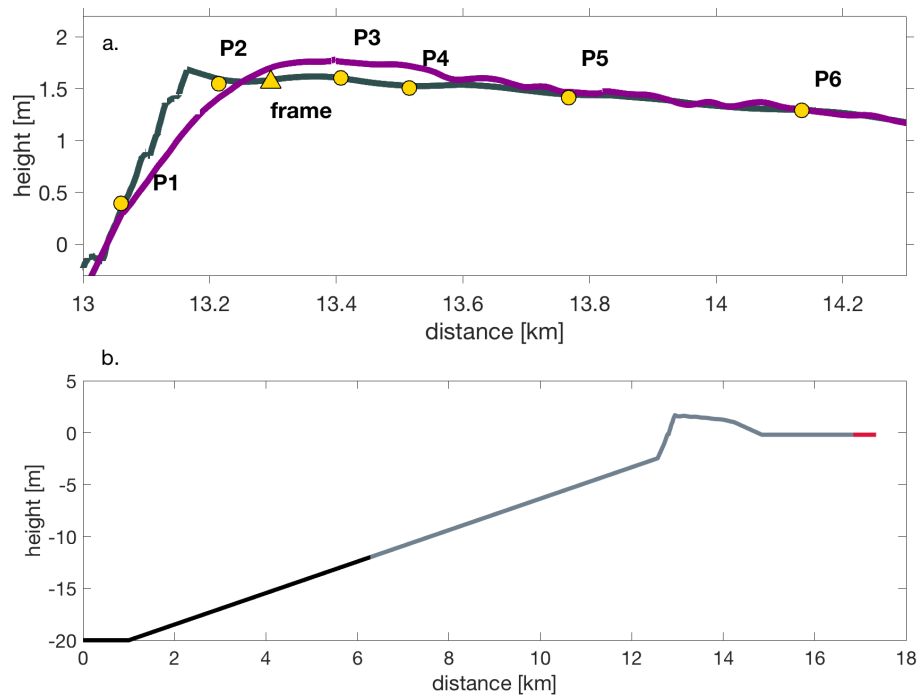


**Figure 2.** The initial (grey) and final (magenta) cross-shore profile for the observations (a). The yellow dots show the location of the pressure sensors and the triangle indicates the instrument frame. The profile for the model-data comparison (b). SWASH was first run to 12 m water depth (dark grey profile) and in a second run from 12 m depth to the back barrier basin (see text for more explanation). The red line indicates the sponge layer.

The instruments consisted of six standalone pressure sensors and an instrument frame, which was equipped with a sideways oriented Sontek Acoustic Doppler Velocimeter Ocean (ADVO) probe to measure flow velocities and a Pressure Transducer (PT). Offshore wave heights and periods were measured hourly by a wave buoy (Schiermonnikoog Noord) located at a water depth of ~20 m approximately 15 km northwest of our field area. Water levels offshore were recorded every 10 min at a tidal station (Huibertgat) in ~5 m depth, approximately 6 km to the North-East, while water levels in the Wadden Sea were collected by the tidal station Schiermonnikoog located ~10 km to the West.

### 2.2.2. Boundary Conditions

Wave and water level boundary conditions on the ocean side were implemented with observations from the offshore stations (Figure 1) as follows. First, wave heights and periods (Table A1) were used to run the model from 20 m to 12 m water depth on a 2 m horizontal grid (Figure 2b) with a JONSWAP spectrum to which a second order bound long wave was added. Second, the simulated water-level time series in 12 m water depth were used as ocean side boundary conditions for consecutive model runs on a 0.5 m horizontal grid, since we prescribed water-level time series at the basin side (described below).

Observations showed that mean water levels in the Wadden Sea were oftentimes higher than in the North Sea during inundation events [7,8] even before high tide, leading to the complete inundation of the field area. This means that, in order to adequately model the inundation of barrier islands in the Wadden Sea, water level gradients need to be included in model runs. To be able to do this in SWASH, the water level in the basin was prescribed as a time-series at the basin boundary. Since we only simulated snapshots in time, this “time-series” was in reality only a repeated value, which was the difference in mean water levels between North and Wadden Sea (as an addition to the implemented still water level). The input file for the basin boundary was created so that it matched the input (water-level time series) file at the ocean side for which the frequency was 0.1 s over a period of 2 h (to allow for enough spin-up time and propagation through the domain). For example, if the mean water level in the Wadden Sea was 0.15 m higher than in the North Sea, the input file at the basin boundary consisted of 72,000 values containing the number 0.15, which the model then added to the still water level at the basin boundary.

### 2.2.3. Introduction of Scenarios for SWASH Computations

For the experiments, first a reference case was chosen which was run on a variation of bed slopes to investigate the effect of island geometry on sediment suspension and transport. Then, the influence of hydrodynamic forcing and inundation depths on the transport processes were explored. The details are outlined below.

As the reference case for the simulations, we chose the most energetic inundation event observed with significant wave height  $H_s = 7.45$  m and peak period  $T_p = 10.1$  s (case R, Table A1), since it was identified as a flow driven event before high tide [7]. The water level at the ocean side was chosen as 2.5 m, which was the water level at high tide and is an upper bound. The water in the basin was chosen to be 0.15 m higher than on the ocean side (2.65 m). This represents a somewhat conservative value for the basin, since water levels were observed to be on average 0.19 m higher in the Wadden Sea than in the North Sea during the two hours before high tide. The model was run on a simplified bottom profile (Figure 3) with a 1:120 slope seaward of the island crest, defined as gentle slope, and a very lightly (~1:2000) down-sloping island top landward of the island crest. The choice of a 1:120 seaward slope was made as an average lower bound for slope steepness on barrier islands in the Netherlands as it was measured at the field site [7,8], while the landward sloping island top was typical at the field location (Figure 3).

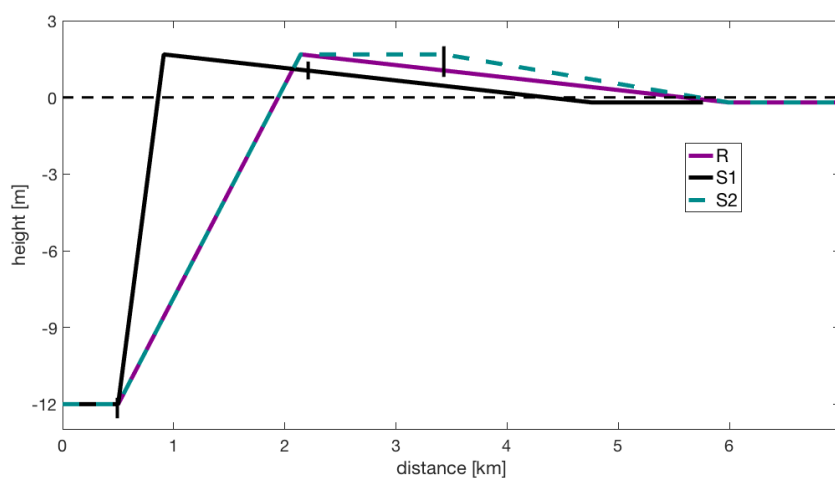


**Figure 3.** The seaward and landward slope configurations for R, S1, and S2 used for the simulations. The vertical black bars indicate the extend of the normalized grid, used in the ensuing figures in Section 3, from the start of the slope until 1.3 km after the crest.

In order to evaluate the effects of slope steepness on sediment stirring and transport, the seaward slope was first changed to 1:30 as an upper bound for beach steepness in the Netherlands (for example, the beach slope at Egmond aan Zee, the Netherlands, ranges between 1:20 and 1:40, [14]), while all other parameters were kept the same (case S1, Table 1). Second, the slope steepness was again set to 1:120 while the island was changed from a down-sloping island top to a straight top (no tilt), to estimate the effect of island geometry (case S2, Table 1).

**Table 1.** Experiments <sup>a</sup>.

	<i>R</i>	<i>S1</i>	<i>S2</i>	<i>H</i>	<i>R</i> <sub>55</sub>	<i>H</i> <sub>55</sub>	<i>L</i>
<i>H</i> <sub>s</sub> (m)	7.45	7.45	7.45	4.55	7.45	4.55	7.45
<i>T</i> <sub>p</sub> (s)	10.0	10.0	10.0	7.2	10.0	7.2	10.0
wl N-Sea (m)	2.5	2.5	2.5	2.5	2.5	2.5	2.0
wl W-Sea (m)	2.65	2.65	2.65	2.65	3.05	3.05	2.15
seaward slope	1:120	1:30	1:120	1:120	1:120	1:120	1:120
landward slope	1:2000	1:2000	0	1:2000	1:2000	1:2000	1:2000

<sup>a</sup> Boundary conditions for the reference case *R*, moderate wave height *H*, lower inundation depth *L*, higher basin water level *H*<sub>55</sub> and *R*<sub>55</sub>, and slope variations *S1* and *S2*. These were defined by significant wave heights (*H*<sub>s</sub>), periods (*T*), water levels in the North Sea (wl N-Sea) and Wadden Sea (wl W-Sea), and slope configurations (see Figure 2).

Observations showed that the sediment transport after high tide oftentimes developed into an episodic regime during which sediment suspension and transport was observed on infragravity wave time scales, due to a further increase in water levels in the Wadden Sea which decreased flow velocities. To investigate this, the reference case *R* was compared to conditions with a basin water level which is 0.55 m higher than the water level on the ocean side (case *R*<sub>55</sub>, all other parameters being the same as *R*). This value was the maximum observed difference between North and Wadden Sea and is here used as an upper bound.

The significance of the wave forcing was evaluated by comparing *R* to wave conditions observed during the inundation with the lowest measured wave heights (*H*<sub>s</sub> = 4.55, *T*<sub>p</sub> = 7.2 s, case *H*, Tables 1 and A1). All other parameters were kept the same as for *R* so that sediment transport under variations in wave forcing could be evaluated independent of water levels or gradients therein. In addition, note that while on average offshore wave heights and water levels in the basin increase with storm size in the North Sea [12], larger waves do not necessarily coincide with stronger gradients (compare flooding 1 and flooding 2 in Table A1). *H* was, like *R*, compared to the maximum water level in the basin (case *H*<sub>55</sub>) to investigate the difference in moderate and strong wave forcing on the local water level gradient. Finally, the water level on the ocean side was lowered by 0.5 m in case *L*, but otherwise parameters were kept the same as for *R*, to explore the influence of inundation depth on sediment suspension and transport. Shallow inundation depths occur either during the tidal cycle or if the storm surge level is lower.

### 3. Results

#### 3.1. Reference Case

For an easier comparison of variations in slope steepness, all experiments will be presented on a “normalized” grid, *xx*, for which output locations are chosen to be at the same depth with respect to mean sea level (MSL). The exception is *S2* for which the water depth stays the same after the crest. For example, *xx* = 0 corresponds to *z* = −12 m (MSL) and *xx* = 1, the location of the crest, is at 1.8 m. For *S2*, this height will stay constant, while for all other slopes the island height drops to 1 m (*xx* = 3.7). After the crest *xx* has the same distance from the crest for all cases, see also (Figure 3).

The transport processes differed considerably from the outer surf zone (starting at *xx* = 0 in a water depth of ~14 m) to the back barrier basin (*xx* = 3.7, water depth = 1.7 m) for reference case *R* (Figure 4a). On the outer slope, the consistently landward directed transport by short wave skewness

$q_{short}$  and asymmetry  $q_{shortA}$  was opposed by the seaward directed mean flow  $q_{mean}$  and infragravity wave transport  $q_{ig}$ . However, landwards of  $xx = 0.75$  in a water depth of  $\sim 3.5$  m all transport was onshore directed. The transport terms will be discussed in detail below. Due to the uncertainty in coefficients and the overestimation of IG waves, we will not discuss absolute values and focus in the remainder of this manuscript on changes and comparisons in a relative sense.

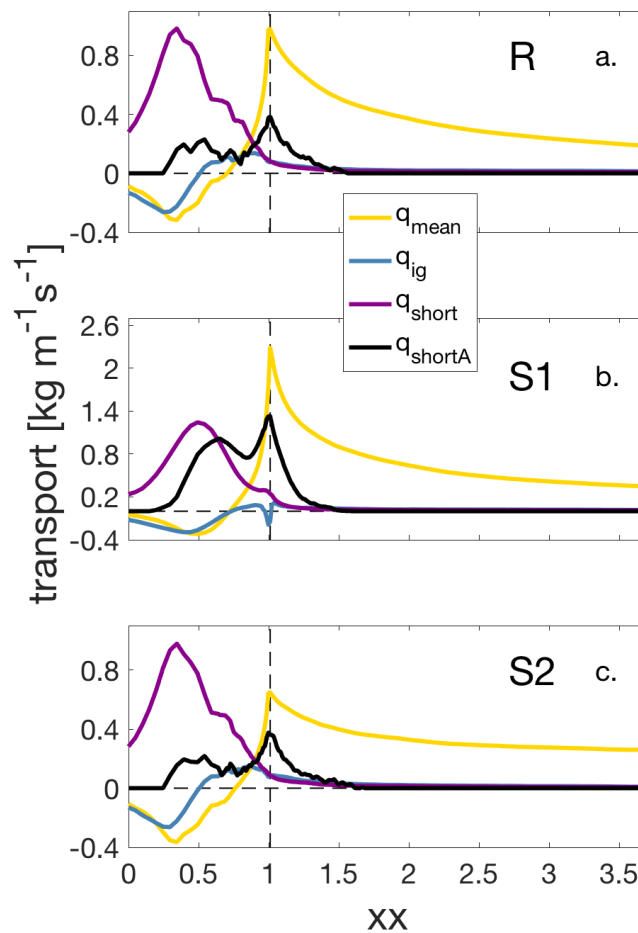


**Figure 4.** Transport processes  $q_{mean}$ ,  $q_{short}$ ,  $q_{ig}$ , and  $q_{shortA}$  are shown for slopes R (a), S1 (b) and S2 (c) on a normalized grid ( $xx$ ) from the beginning of the seaward slopes ( $xx = 0$ ) to the back barrier basin ( $xx = 3.7$ ). Grid locations before the crest (indicated by the vertical dashed line) indicate output in the same water depth (but not the same distance in reference to the crest, while they are equidistant after the crest (and at the same depth for R and S1, but not for S2, see Figure 2). Note that vertical scales are different.

The term  $q_{short}$  increased from the start of the slope ( $xx = 0$ ) to a maximum on the outer slope (Figure 4a) at the onset of wave breaking in a water depth of 9.8 m, corresponding to the shoaling of short waves (Figure 5d) which caused an increase in wave skewness (Figure 6a). Due to wave breaking,  $q_{short}$  was significantly smaller at the crest and close to zero after it ( $xx = 1.5$ ).  $q_{short}$  was mostly stirred by the short waves themselves (Figure 7b), with the exception of a small contribution to the stirring by IG waves (max  $\sim 30\%$  of total short wave transport after the crest when short wave stirring is small, not shown).

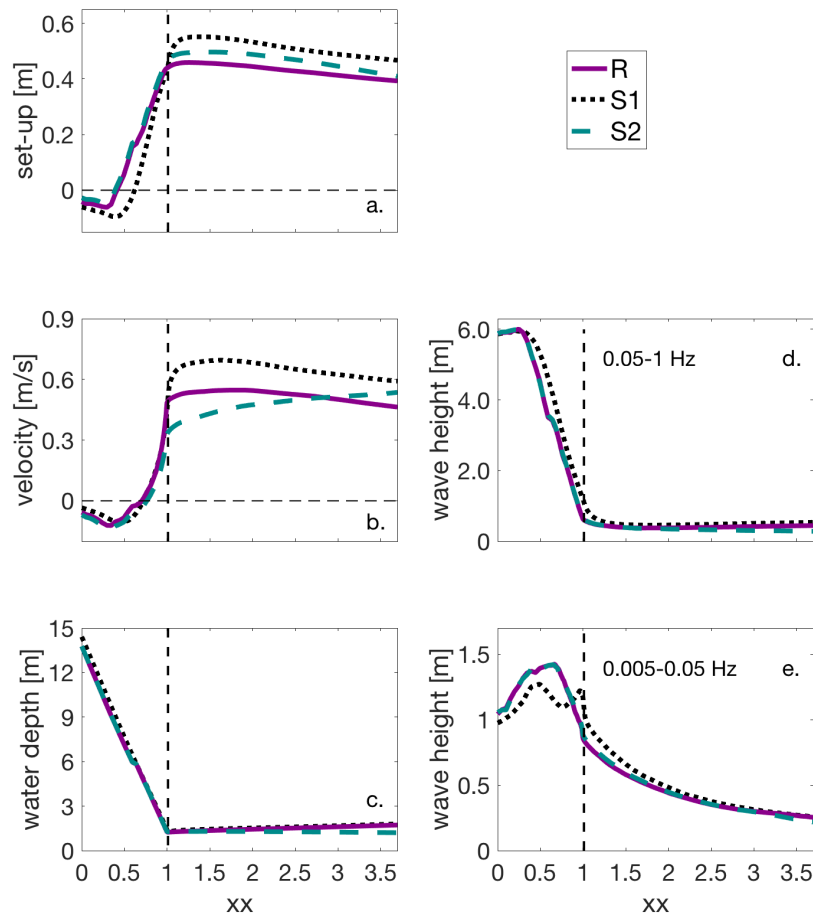


**Figure 5.** Modeled water level set-up (a) which includes elevated water levels in the basin, mean flow velocity (b), water depth (c, including storm surge and wave set-up), short (d) and infragravity (IG) (e) wave heights and water depth for slopes R, S1 and S2 on a normalized grid (xx) from the beginning of the seaward slopes (xx = 0) to the back barrier basin (xx = 3.7). Grid locations before the crest (indicated by the vertical dashed line) indicate output in the same water depth (but not the same distance in reference to the crest), while they are equidistant and at the same depth after the crest for R and S1 (but not for S2 for which the island top has the same height as the crest).

Transport due to short-wave acceleration skewness  $q_{shortA}$  developed on the outer slope ( $\sim xx = 0.5$ ), caused by an increase in velocity asymmetry (Figure 6b). While short-wave height at the crest is only about 1/10 of the outer surfzone values, short-wave asymmetry is at a maximum (Figure 6b) due to the limited water depths over the crest. Since accelerations are largest under the steep wave crest where orbital velocities are onshore directed, the net transport by acceleration skewness will be onshore directed [31].  $q_{shortA}$  exceeded  $q_{short}$  at the crest by far, which could at least partly depend on our choice of parameters. However, the trend is consistent with the change in wave shape, which showed a decline in short wave skewness and the before mentioned maximum in asymmetry at the crest (Figure 6a,b).

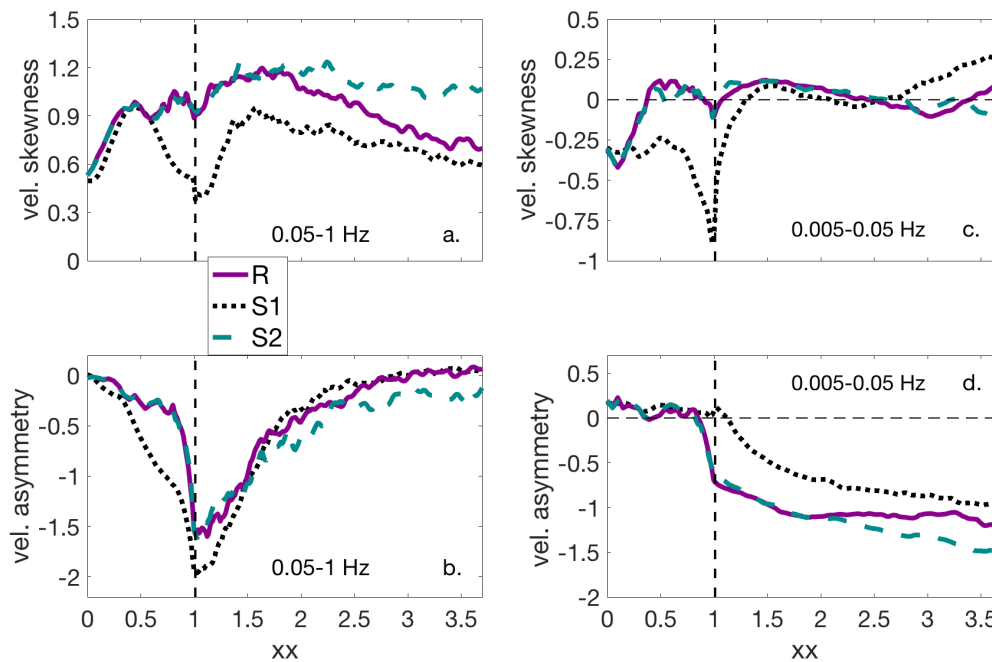


**Figure 6.** Modeled short wave velocity skewness (a) and asymmetry (b), and IG wave velocity skewness (c) and asymmetry (d) for slopes R, S1 and S2 on a normalized grid ( $xx$ ) from the beginning of the seaward slopes ( $xx = 0$ ) to the back barrier basin ( $xx = 3.7$ ). Grid locations before the crest (indicated by the vertical dashed line) indicate output in the same water depth (but not the same distance in reference to the crest), while they are equidistant and at the same depth after the crest for R and S1 (but not for S2 for which the island top has the same height as the crest).

The term  $q_{ig}$  was offshore directed on the outer slope (Figure 4), and onshore thereafter ( $\sim xx = 0.5$ ). The maximum of the seaward directed  $q_{ig}$  was located almost at the same location as the maximum for  $q_{short}$  ( $xx \sim 0.3$ ) and was caused by the more intense short-wave stirring at this location (Figure 7b).  $q_{ig}$  decreased around the crest, probably because of a decrease in short wave stirring. The change in transport direction for  $q_{ig}$  suggests that in the shoaling zone, where IG waves are bound to the wave group, the larger short waves coincide with the seaward stroke of the IG waves (e.g., [15,35]). After the bound IG wave is released during short wave breaking, the larger short waves coincide with the positive stroke of the IG waves, which is probably caused by depth modulation of the infragravity waves [15,36,37]. The large reduction in IG wave heights of  $\sim 60\%$  between the maximum  $q_{ig}$  on the seaward slope and values at the crest suggests IG wave breaking as indicated by e.g., Van Dongeren et al. [13] and De Bakker et al. [14], but could also have been at least partly caused by bed friction or nonlinear energy transfers from IG- to short waves. Estimates of IG wave dissipation during inundation—based on earlier field experiments [8]—suggested that IG wave breaking before the crest was roughly 2–9 times higher than IG wave dissipation by bed friction, depending on the water depth. The contribution of IG wave stirring to  $q_{ig}$  is close to zero (Figure 7b), since IG waves skewness is small (Figure 6c), even though asymmetry is high (Figure 6d).

The term  $q_{mean}$  was largest around the crest and was reduced to  $\sim 25\%$  of the crest value at the basin side. While flow velocities were highest after the crest ( $xx \sim 1.5$ ), the maximum in  $q_{mean}$  at the crest was caused by short and IG wave stirring (Figure 7a) which continued to be an important contributor even after the crest. As mentioned before,  $q_{mean}$  changed direction from seaward (where it was solely stirred by short waves) to landward directed about mid-surfzone at  $xx = 0.75$ . On a closed beach, the mean seaward directed flow (undertow) is generated to balance the landwards directed mass flux under the breaking wave crests. Symonds et al. [38] found for a reef situation (which is similar to inundation on a barrier island in that the landward boundary is open) that the radiation

stress gradient, caused by the breaking waves, is partitioned between setting up the water level and driving a cross-shore flow. Here, it appears that the (small) offshore directed flow is a result of the strongest short wave breaking in the outer surfzone which created a steep seaward directed pressure gradient and forced the seaward flow. After the crest, wave breaking ceased and the flow was forced by the landward directed pressure gradient (Figure 5b).

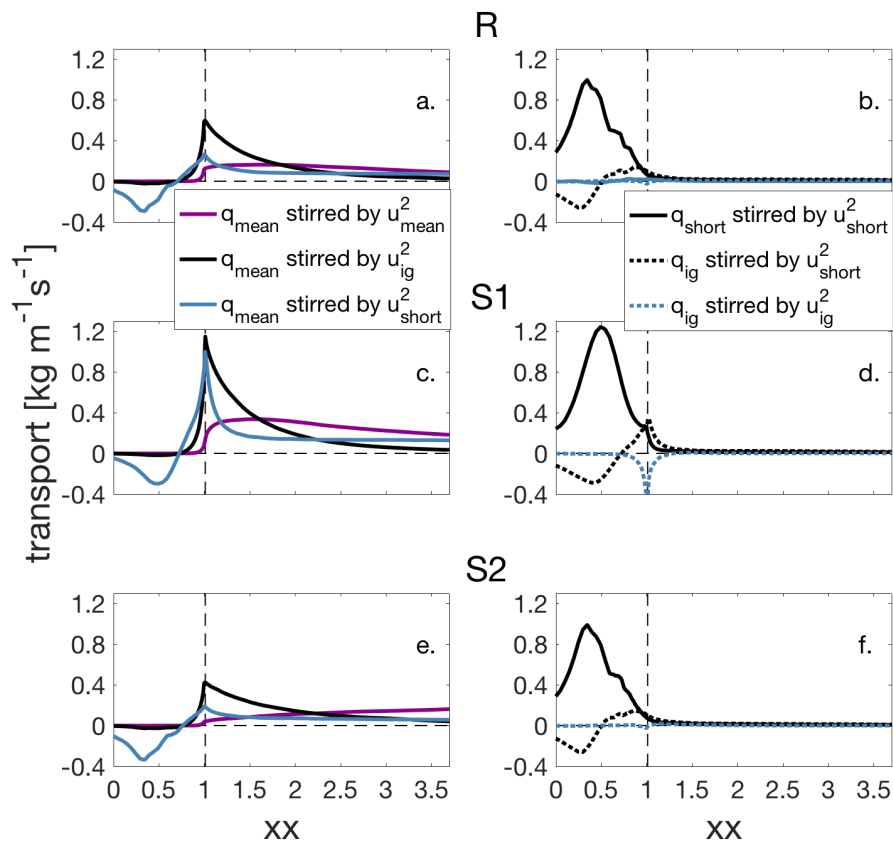


**Figure 7.** Stirring processes for  $q_{mean}$  (a,c,e),  $q_{short}$  (b,d,f) and  $q_{ig}$  (b,d,f) for R (a,b), S1 (c,d) and S2 (e,f) on a normalized grid ( $xx$ ) from the beginning of the seaward slopes ( $xx = 0$ ) to the back barrier basin ( $xx = 3.7$ ). Grid locations before the crest (indicated by the vertical dashed line) indicate output in the same water depth (but not the same distance in reference to the crest), while they are equidistant and at the same depth after the crest for R and S1 (but not for S2 for which the island top has the same height as the crest).

Stirring for  $q_{mean}$  before the crest is exclusively provided by short and IG waves and continued to be relevant even after the crest (Figure 7a), since wave energy was not completely dissipated (Figure 5c,d,e). Even though IG wave stirring is surely overestimated, these results agree with observations for which increases in sediment suspension on IG time scales was observed [7].

### 3.2. Slope Comparisons

The comparison of reference case R with S1 (slope of 1:30, everything else being the same as R), suggests that transport is generally higher for the steeper slope. The maximum for  $q_{short}$  on S1 was located more shorewards in a water depth that was approximately 3 m lower than for R.  $q_{short}$  was about 30% higher for the steeper slope compared to the gentle slope due to higher short waves (Figure 5d). On the crest, however, where short waves on the steep slope were almost twice as high as on the gentle slope (1 m compared to 0.6 m),  $q_{short}$  was about 3 times as high for S1 as it was for R. This is reflected in the higher stirring for the short wave transport (Figure 7b,d) which is again almost

entirely forced by the short waves (the very small contribution of IG wave stirring is not shown). The difference in transport and stirring for  $q_{short}$  can be explained by the effect of slope steepness on wave transformation, as was shown in previous studies (e.g., [39]). Since on a steeper slope less wave energy will be dissipated (Figure 5d), short-wave heights were much larger for S1. Lower skewness and higher asymmetry for S1 values suggest (Figure 6a,b) that, while short waves dissipated less energy, they were more pitched forward. This is reflected in  $q_{shortA}$ , which is about 4–5 times higher on the steep slope compared to the gentle slope (Figure 4b). Generally, the results suggest that short waves transport more sediment from the surfzone over the crest onto the island top for steeper slopes.

The evolution of  $q_{ig}$  was obviously different between the slopes. While on the gentle slope  $q_{ig}$  is landward directed from  $\sim xx = 0.5$  (Figure 4), on the steeper slope, most of the transport in the inner surfzone and at the crest was seaward directed. The seaward directed  $q_{ig}$ , stirred by IG waves, at the S1 crest contrasted with  $R$  (Figure 7d), which was close to zero. At the same location, landward directed  $q_{ig}$  stirred by short waves was predicted to be about three times higher than for  $R$ . The difference in  $q_{ig}$  between  $R$  and S1, again, was caused by the difference in wave transformation on the gentle and the steep slope. IG waves grew more on the gentler outer seaward slope compared to the steeper slope, probably because energy transfers between IG waves lead to a steepening of these waves followed by wave breaking [18]. Furthermore, IG waves apparently broke only right before the crest on the steeper slope and were higher by roughly 10% at the crest than IG waves on  $R$ . For S1, strong (−0.8) negative IG wave skewness (Figure 6c) was predicted at the crest, which indicates that IG waves had broader, shallower crests and steeper narrower troughs. During negative IG wave skewness, the seaward stroke velocity is faster than during the landward stroke, which might explain the seaward contribution of IG suspended  $q_{ig}$  transport. Butt and Russell [40] found negative skewness in the swash during high energy conditions and related potentially offshore directed transport to it. Negative IG wave skewness was also predicted for  $R$  around the crest (albeit close to zero) and was observed for field measurements (Figure A1). The landward directed component of short wave suspended  $q_{ig}$  can, again, be related to higher short waves suspending more sediment during the landward stroke of IG waves.

Prediction for the seaward directed mean flow transport  $q_{mean}$  in the outer surfzone were similar for  $R$  and S1 (compare Figure 4a and Figure 4b), but the landward  $q_{mean}$  increased at a higher rate for S1 and was more than double at the crest and on the island top. Since flow velocities were the same on the slope, the higher values before and at the crest can be foremost attributed to increased IG and short wave stirring (Figure 7c) caused by the larger wave heights (especially for IG waves, Figure 5c,d). Higher  $q_{mean}$  for S1 on the island top is forced by continuous wave breaking over the crest, which moved the location of maximum set-up for S1 landwards to around  $xx = 1.25$  and increased it roughly 25 % compared to  $R$ . Furthermore, mean velocities were  $\sim 30\%$  higher after the crest. In general, mean flow velocities in an open boundary system are forced by breaking waves and pressure gradients. The similar mean flow velocities before and at the crest might have been a result of a balance between the seaward directed pressure gradient which was steeper for S1, inducing a stronger seaward flow component for S1, and higher onshore velocities induced by wave breaking.

In comparison,  $q_{mean}$  on S2 (with a straight island top instead of a downward slope) was predicted as only  $\sim 60\%$  of  $R$  at the crest, but  $\sim 130\%$  of  $R$  at the basin side (Figure 4a,c). This coincided with smaller mean flow velocities at and after the crest as for  $R$ ; however, velocities increased from crest to back barrier basin for S2, while they decreased for  $R$ . These differences were likely caused by the relative higher decrease in water depth towards the basin (since the elevation of the top stayed the same) compared to  $R$ , which forced flow velocity to increase to conserve discharge. Since the mean flow was increasing toward the basin side, this suggests that more sediment will be transported into the basin compared to a sloping top. In return, this would indicate that, under the same wave forcing and beach slope steepness, more sediment can be accreted on the island for steeper sloping island tops.

Results suggest that waves directly dominate the sediment transport processes before and at the crest through transport and by providing the necessary stirring for  $q_{mean}$ . On the island top, the transport is dominated by the mean flow which is forced by the pressure gradient. In addition,

variations in transport can be introduced by island geometry, such as stronger dissipation on a gentler slope compared to a steeper slope and a decrease in the landward transport for down-sloping island tops through the increase in water depth which reduces flow velocities.

### 3.3. Variations in Hydrodynamic Forcing and Inundation Depths

Section 3.2 discussed the predicted differences in sediment transport under different island geometries. In the following, the influence of hydrodynamic forcing will be explored.

Not surprisingly, when offshore wave heights were reduced by 60% of  $R$  values (case  $H$ ), it caused an overall decrease in transport compared to  $R$  (compare Figure 8a and Figure 8b). While  $q_{ig}$ ,  $q_{shortA}$ , and  $q_{short}$  for  $H$  were roughly 1/3 to 1/2 of  $R$  values,  $q_{mean}$  was severely reduced to about 1/6 of  $R$ . The smaller set-up for  $H$  (Figure 9a), due to the smaller wave forcing, balanced the water levels in the back barrier basin. Therefore, forcing by the pressure gradient on the landward side was missing and transport was small, since flow velocities were close to zero (0.05 m/s, Figure 9b). Furthermore, the maximum seaward transport on the slope exceeded the maximum landward directed transport (Figure 8b), due to slightly higher flow velocities ( $-0.08$  m/s) and more intense short wave stirring on the slope compared to the crest (not shown). Stirring for  $q_{mean}$  was only provided by IG and short waves since the flow velocity was close to zero (not shown). Generally, transport for  $H$  on the slope was initiated higher up on the slope than for  $R$ , due to the lower wave height over depth ratio which caused a later onset of wave nonlinearities.

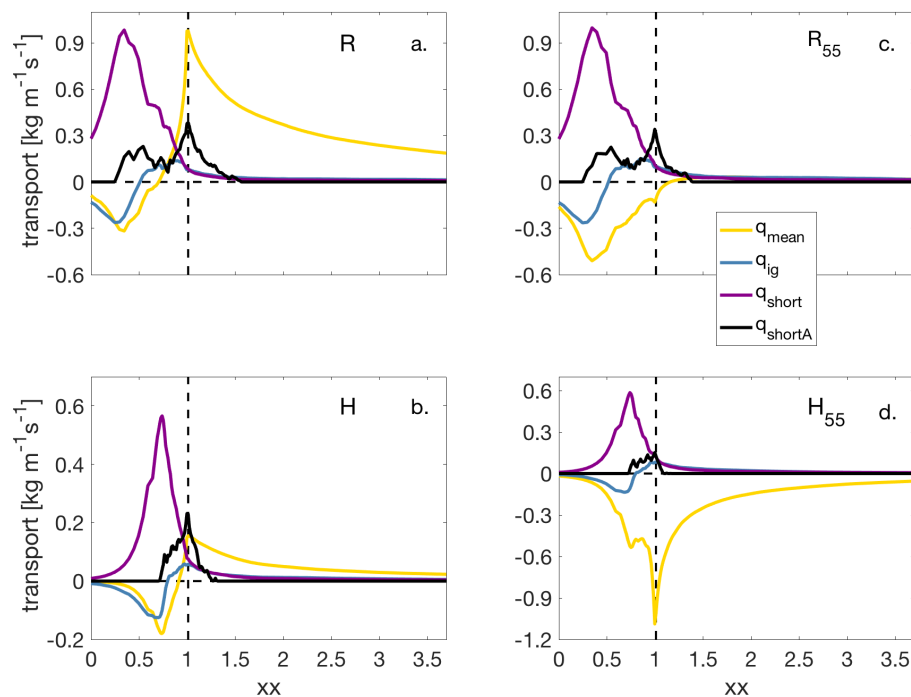


**Figure 8.** Transport processes  $q_{mean}$ ,  $q_{short}$ ,  $q_{ig}$ , and  $q_{shortA}$  are shown for reference case  $R$  ( $H_s = 7.45$  m) (a) and  $H$  ( $H_s = 4.55$  m) (b). For  $R$  and  $H$  the water level in the basin was 0.15 m higher than offshore while it was 0.55 m higher for  $R_{55}$  (c.) and  $H_{55}$  (d). The  $x$ -axis is the normalized grid ( $xx$ ) from the beginning of the seaward slopes ( $xx = 0$ ) to the back barrier basin ( $xx = 3.7$ ). Here, the slopes are the same (1:120) and output at all grid locations is in the same water depth. The vertical dashed line indicates the location of the crest.

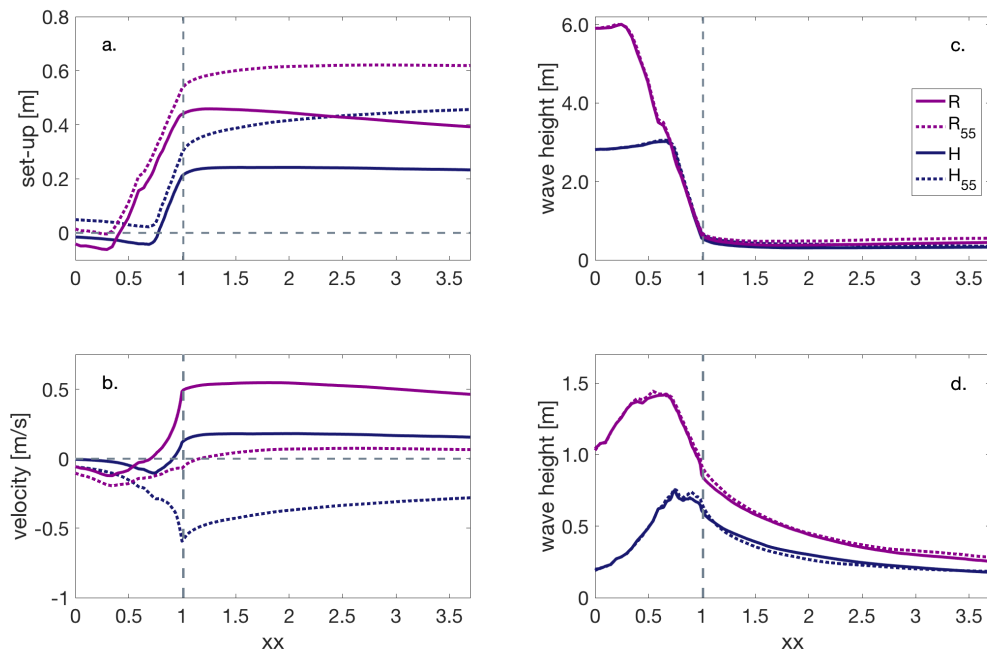


**Figure 9.** Predicted water level set-up (which includes higher water levels in the basin) (a), mean flow velocities (b), short- (c) and IG wave heights (d) for R, H, R<sub>55</sub>, and H<sub>55</sub>. The extension 55 refers to a water level that is 0.55 m higher in the back barrier basin. The x-axis is the normalized grid (xx) from the beginning of the seaward slopes (xx = 0) to the back barrier basin (xx = 3.7). Here, the slopes are the same (1:120) and output at all grid locations is in the same water depth. The vertical dashed line indicates the location of the crest.

To explore the balance between wave-induced set-up and higher water levels in the back barrier basin further (and its impact on sediment transport), water levels in the back barrier basin were increased for R and H so that they were 0.55 m higher than on the ocean side (cases R<sub>55</sub> and H<sub>55</sub>). The increase in water levels for case R<sub>55</sub> affected mostly  $q_{mean}$  and caused it to be seaward directed between the outer surfzone and  $\sim xx = 1.25$ . Maximum seaward directed  $q_{mean}$  values were almost twice as high for R<sub>55</sub> as for R (compare Figure 8a and Figure 8c) in the outer surfzone. Wave set-up did not exceed the higher water levels in the basin and was a couple of centimeters smaller so that the water level gradient was offshore directed (Figure 9a), even though the flow did not reverse to a seaward direction landwards of the crest and was close to zero (Figure 9b). The small landward directed mean flow velocity was probably forced by the skewed orbital motions, while the IG radiation stress gradient might have contributed.  $q_{mean}$  completely reversed to a seaward direction for lower wave heights, as can be seen for H<sub>55</sub> (Figure 8d). Here, the wave set-up was too small (Figure 9a) to oppose the higher water levels in the basin and a continuous seaward directed water level gradient was created, driving strong seaward flow throughout the domain.

Model predictions suggest that a critical threshold exists between water level set-up and higher basin levels which determines the mean-flow transport direction, and this threshold depends on the offshore wave forcing. This is in agreement with observations and model results of cross-shore flow velocities during inundation [8,12]. Clearly, in situations when the water level in the basin is lower than in the ocean, as can be observed at times during the rising tide in the Netherlands due to a phase lag between ocean and basin,  $q_{mean}$  will always be landwards directed (as was observed).

What is striking is that  $q_{shortA}$  was reduced by approximately 35% for  $H_{55}$  on the crest in comparison to  $H$  (compare Figure 8b and Figure 8d), while it is only reduced by  $\sim 10\%$  for  $R_{55}$ . This is in line with a reduction in short wave asymmetry which was  $\sim -1.2$  and  $-0.8$  for  $H$  and  $H_{55}$ , while, for  $R$  and  $R_{55}$  wave heights, asymmetries were  $-1.5$  and  $-1.3$ , respectively. This difference in wave shape transformation might be explained by the water depth to wave height ratio, since set-up was greater for the higher wave case.

Generally, lowering the ocean side water level (case  $L$ ) while keeping the basin side level 0.15 m higher in the basin, also shows an overall increase in  $q_{shortA}$  (Figure 10) which is roughly 30% higher at the crest than  $R$ . Here, short wave height asymmetries were as high as 2.1 (not shown). In addition to  $q_{shortA}$ ,  $q_{mean}$  also increased for lower inundation depths (25% higher at the crest). The increase in seaward directed  $q_{mean}$  before the crest was forced by slightly higher seaward directed velocities (Figure 11b). While the set-up for  $L$  was higher (Figure 11a) due to the lower water depth, velocities on the island top were only slightly larger than for  $R$  and smaller at the crest. The  $\sim 20\%$  higher  $q_{mean}$  for  $L$  was caused by an increase in IG stirring (not shown), which could have been forced by slightly higher wave skewness at the crest (0.06 for  $R$  and 0.12 for  $L$ ) or by a higher radiation stress gradient, since IG wave heights were slightly lower for  $L$ .  $q_{mean}$  stirred by short wave on the other hand was slightly lower after the crest, since wave heights for  $L$  were close to zero due to the low inundation depths ( $\sim 0.8$  m at the crest).

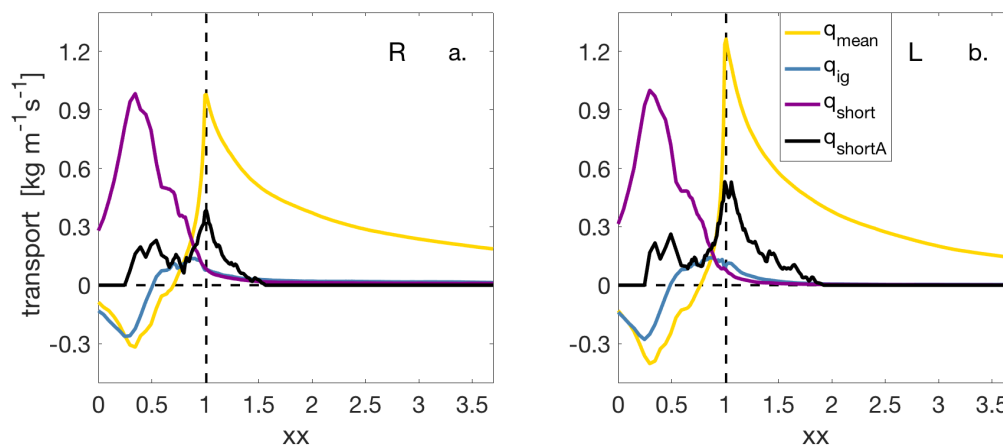


**Figure 10.** Transport processes  $q_{mean}$ ,  $q_{short}$ ,  $q_{ig}$ , and  $q_{shortA}$  are shown for reference case  $R$  (a) and case  $L$  (b) for which the water level at the ocean side was lowered by 0.5 m. The  $x$ -axis is the normalized grid ( $xx$ ) from the beginning of the seaward slopes ( $xx = 0$ ) to the back barrier basin ( $xx = 3.7$ ). Here, the slopes are the same (1:120) and output at all grid locations is in the same water depth. The vertical dashed line indicates the location of the crest.

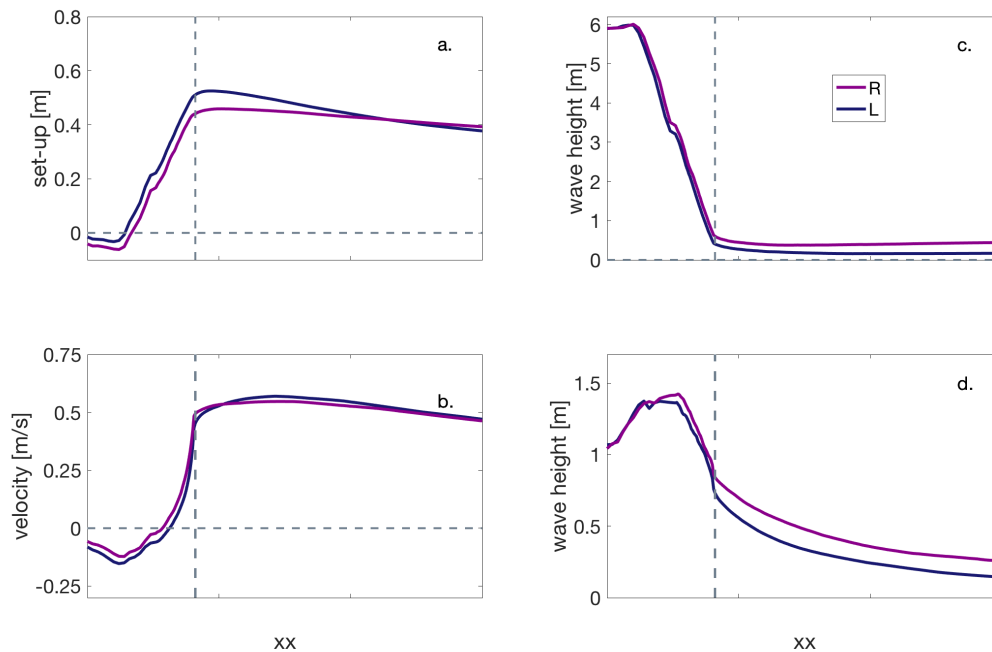


**Figure 11.** Predicted water level set-up (which includes higher water levels in the basin) (a), mean flow velocities (b), short- (c) and IG wave heights (d) for R and L. The  $x$ -axis is the normalized grid ( $xx$ ) from the beginning of the seaward slopes ( $xx = 0$ ) to the back barrier basin ( $xx = 3.7$ ). Here, the slopes are the same (1:120) and output at all grid locations is in the same water depth. The vertical dashed line indicates the location of the crest.

#### 4. Discussion

##### 4.1. Role of Waves and Mean Flow throughout the Domain

Model results suggest that stirring and transport by short waves is most important on the outer slope, after which  $q_{short}$  decreases significantly. On the other hand,  $q_{shortA}$  usually increases from the outer slope and is maximum at the crest. While most terms increase with an increase in slope steepness,  $q_{ig}$  varies most in magnitude and direction. The switch from a seaward to a landward transport direction between outer to inner surfzone had been noted before by De Bakker et al. [15] for short-wave stirred IG transport on a closed beach. The seaward directed  $q_{ig}$  at the crest of the steep slope is likely an effect of the negative IG wave skewness, which is much higher on the steeper slope. While negative skewness was observed by others and appears to be related to potential offshore IG transport [40,41], the nonlinear processes which are causing it and their slope dependence need to be further investigated. While in most cases, these processes will generally be rather small compared to  $q_{mean}$  and  $q_{shortA}$  (especially in light of the IG wave overprediction), negative IG skewness might determine the net seaward or landward transport direction when mean flow velocities are small, such as for  $R_{55}$ .

Engelstad et al. [7] found two transport regimes at their field site, located at the island crest of a barrier island in the North Sea: a flow driven regime during high flow velocities ( $>0.5$  m/s), and an episodic regime for low flow velocities, where sediment suspension and suspended transport was observed on an IG wave time scale. Results suggest that this finding might be generally applied, since the mean-flow rarely stirs sediment if it is  $<0.5$  m/s (compare Figure 2 and Figure 5), and most of the stirring is provided by IG and short waves. The difference in the velocity threshold for the slopes is caused by the fact that waves dissipate less energy on the steeper slope and continue to provide much of the stirring for  $q_{mean}$  after the crest. While it was unclear in that study if the observed high values of suspended sediment under IG waves were caused by the IG waves themselves or forced by larger

short waves riding the crest of IG waves, model results suggest that IG wave stirring is important, especially landwards of the crest when most of the short wave energy has dissipated.

#### 4.2. Implications for Barrier Islands

The wave climate, tidal- and storm forcing, and island geometry vary for locations. In the North Sea region, winter storms regularly cause elevated water levels in the Wadden Sea. Observations, however, showed that seaward flow and sediment transport on the island top was small [7,8], since wave heights were large enough to create significant wave set-up opposing the seaward directed large scale water level gradients. This was also reflected in model results where large wave heights were able to prevent the flow reversal on the island top, even though the magnitude of the seaward directed water level gradient was the highest measured (0.55 m) during the observational period (see, e.g.,  $R$  and  $R_{55}$  in Figure 9). In a system with smaller wave heights such as in the Gulf of Mexico during cold fronts, tropical storms or even weak hurricanes where offshore wave heights rarely exceed 4 m [19], wave set-up will be rather small (Figure 9). This will generally decrease deposition on the island top, but also in the basin. However, if the water level in the basin is large enough, such as during the surge-ebb caused by passing hurricanes, erosion of the island top and seaward deposition will occur (see  $H$  and  $H_{55}$  in Figure 8), as predicted and observed by Sherwood et al. [9], Harter and Figlus [10], Goff et al. [42]. This suggests that islands that are exposed to small wave forcing, and large seaward directed water level gradients will be more vulnerable to erosion.

Generally, the results imply that, while the cross-shore geometry is important for the island response to inundation, considerations for the restoration of barrier island and overwash processes need to consider the local wave climate and surge levels in the back barrier basin as well.

#### 4.3. Model Performance and Sensitivity of Results to Model Implementations

The model captured observed changes in water levels and short wave heights well (for a detailed model-data comparison, see Appendix A), but flow velocities were underpredicted while infragravity wave heights were overpredicted. Furthermore, asymmetry and skewness were not captured well, which can be foremost ascribed to the comparison of field data with the 1D mode of SWASH. In particular, the transformation of IG skewness is unsatisfactory, likely since the skewness changes further seaward in the model results compared to the observations from negative to positive, in addition to strong observed variations in the observed skewness. These were likely caused by local factors in the field. Short wave asymmetry and skewness were limited to the frequency range 0.05–0.3 Hz, since observations showed that short waves generated in the Wadden Sea were propagating seaward. These might have affected the wave shape and sediment stirring; however, since no significant morphological changes were observed at the Wadden Sea side [7,8], their effect is probably small. Discrepancies between model and observations should not effect the general conclusions of our results, since we only compare each transport term in a relative sense for changes in island geometry and forcing. However, it would be of interest to be able to compare the magnitude of each forcing term with each other to find the relative importance of each term. Hopefully, this will be addressed in future research.

Our results were affected by the choices we made (a) in the SWASH implementations, and (b) in the use of parameters for the transport models. SWASH in 1D mode leads, as mentioned earlier, to an overestimation of IG waves, and therefore transport and stirring by infragravity waves is surely overestimated. Furthermore, since we had no means to fit the parameters for the transport model, we chose values from the literature and combined them to find reasonable predictions for the transport processes. However, the choice of  $\epsilon_b = 1.03$  and  $K_a = 0.37 \text{ kg s m}^{-2}$  is open for debate. Bagnold [28] initially suggested a value of 0.13 for  $\epsilon_b$ , while Bailard [29] set  $\epsilon_b = 0.21$  after calibration to field data. Drake and Calantoni [30] found  $\epsilon_b = 1.03$  for their discrete particle model which is about eight times the value Bagnold [28] originally proposed for steady unidirectional flow. On the other hand, Drake and Calantoni [30] determined  $K_a = 0.07 \text{ kg s m}^{-2}$ , while Hoefel and Elgar [31] attained  $K_a = 0.37 \text{ kg s m}^{-2}$  when comparing model with observational data, which is higher by a factor of 5.

This clearly shows that there is uncertainty in the absolute numbers, and any use of the transport model to estimate the actual transport would require careful calibration. However, the acceleration under the steep faces of asymmetric waves is assumed to contribute significantly to sediment transport over bars and in the shallow surfzone [31,43–45], and Brinkkemper et al. [45] found short wave sediment transport to not be related to the short wave skewness in low-energy conditions in the shallow surf zone. Therefore, while the relative importance of the transport terms might be not a hundred percent accurate, their relationship seems realistic, which allowed us to investigate how sediment transport processes are influenced by bed slopes and hydrodynamic forcing.

Additionally, it is noteworthy that the modeling results reflect processes for an area which is missing high dunes or ridges that might impact the sediment transport processes. It is likely that sediment transport in the presence of higher elevation features will differ from our results.

Lastly, our choice of using only the bedload part of the Bailard [29] equation ignores the suspended sediment transport, which was shown to be important during the inundation of a barrier island in the Wadden Sea [7]. During suspended sediment transport, the transport direction can be affected by phase lags between the suspended sediment and the wave velocity. For example, sediment suspended into the water column under the crest (landwards directed velocity) can be transported seaward under the trough if settling is slow [31,46,47]. This was not observed in the field [7], probably because the bed was very smooth and ripples small. This might be different for uneven terrain. Therefore, suspended sediment transport and the possible reversal of transport should be addressed for these cases in future research.

## 5. Conclusions

The non-hydrostatic wave model SWASH was used to investigate the relative importance of bedload transport processes, such as transport by mean flow, short- and IG waves, and acceleration skewness, during barrier island inundation for various island configurations and hydrodynamic forcing. Simulations suggested that the sediment transport processes from the outer surfzone until landwards of the island crest are dominated by the waves. These either transported sediment directly or stirred the sediment for the mean flow transport. Transport by short waves was continuously landwards directed, while IG wave transport was seaward directed in the outer surfzone and landward directed in the inner surfzone, consistent with earlier observations. Landwards of the crest, bedload transport was mostly dominated by the mean flow, which was forced by the water level gradient. A critical threshold exists between wave set-up, which depends on the offshore wave forcing and inundation depths, and basin water levels. These determine the mean-flow transport direction and magnitude in the inner surfzone and on the island top.

Model results suggest that short wave and mean flow transport is enhanced on steeper slopes throughout the domain, since they cause less energy dissipation and higher flow velocities. Further modifications of the island geometries suggested that the the slope of the island top and the width of the island foremost affect the mean-flow transport, while changes in inundation depth will also affect transport by short-wave acceleration skewness.

**Author Contributions:** All co-authors contributed to the initial framework and methodology. A.E. performed the simulations and analysis. The manuscript was written by A.E., while all other co-authors contributed by discussing, editing and improving the paper.

**Funding:** This work was funded by the Netherlands Organisation for Scientific Research (NWO) under contract 850.13.051, as well as by Natuurmonumenten, the National Forest Service (Staatsbosbeheer, SBB), and the Wadden Academy.

**Acknowledgments:** This work is supported by NWO, Natuurmonumenten, the National Forest Service (Staatsbosbeheer, SBB), and the Wadden Academy. The authors would like to thank the anonymous reviewers for their insightful comments and Associate Editor Mila Marinkovic for her help with this publication.

**Conflicts of Interest:** The authors declare no conflict of interest.

## Appendix A

### Appendix A.1. Boundary Conditions and Model Settings

For the model-data comparison, four of the five observed inundation events were used (there was doubt about the measured water levels during the fifth event; Table A1). Observational data were averaged over the first 15 min of each full hour from 2 h before until 2 h after high tide to have five data-points if records were long enough (flooding 1 and 4). Otherwise, three data-points (1 h before to 1 h after high tide) were used (flooding 2 and 3). The 15-minute average was chosen because conditions were not stationary due to the tidally induced changes in water levels.

**Table A1.** Boundary conditions for observed floodings at high tide <sup>a</sup>.

Flooding #	Wind Speed [m/s]	Wind Direction [°]	Wave Hs [m]	Wave T [s]	Wave $\theta$ [°]	Water Level N. Sea [m]	Water Level W. Sea [m]
1	16	270	6.20	8.7	307	2.34	2.52
2	11	300	5.11	8.3	327	1.84	2.19
3	15	310	4.55	7.2	321	2.05	2.16
4	20	330	7.43	10.1	326	2.50	2.92

<sup>a</sup> If dates are listed twice, two inundation events occurred on one day and were separated by a low tide. Wind speed and direction as well as significant wave height (Hs), periods (T) and wave angle ( $\theta$ ) were measured by an offshore meteorological station (Wierumergronden) and a wave buoy (Schiermonnikoog Noord) and were averaged over one hour at high tide. Water levels (wl) in the North Sea (N. Sea, measured at Huibertgat) and Wadden Sea (W. Sea, measured at Schiermonnikoog station) were also averaged over one hour at high tide. The coastline is aligned  $\sim -10$  degrees with true East.

Water levels created the largest uncertainty in the model-data comparison, since offshore water levels were only available relatively close to shore (as mentioned above) in a water depth of roughly 5 m and for the basin at a distance of about 10 km to the west of the field side. While the tidal station Schiermonnikoog is close to the tidal inlet west of the island, the field site was close to the inlet to the east and water levels might not have been the same.

The bottom profile for the model-data comparison (Figure 2b) is a combination of the measured island profile during the instrument deployment and offshore measurements available from Rijkswaterstaat (RWS). The existing bar-trough morphology was simplified to a straight line from 20 to 2.5 m depth and was extended at the seaward and the basin side of the transect (km 0–1 and  $\sim$  km 14–17), resulting in a total domain length of  $\sim$ 17.5 km. A profile measured at the beginning of the campaign (Figure 2a) was used for flooding 1–3, while the final profile survey was used for flooding 4.

In the model data comparison, the best agreement for flooding 1–3 was found with breaking parameter  $\alpha$  set to 0.5 and the criterion for the persistence of wave breaking,  $\beta = 0.25$ , while for flooding 4  $\alpha = 0.4$  and  $\beta = 0.2$  provided best agreement. To account for the high observed cross-shore velocities, Manning’s roughness coefficient,  $n$  was set to 0.14 and 0.1 for floodings 1–3 and flooding 4, respectively.

### Appendix A.2. Model-Data Comparison

To investigate the ability of the SWASH model to hindcast the hydrodynamic conditions observed in the field, we compared observed and modeled water levels, cross-shore velocities, IG and short wave heights during the rising and falling tide for flooding 1 along the instrument transect (Figure A1).

Despite the uncertainty in water levels, modeled and observed water levels agree well (Figure A1a,e,i) during different tidal stages. The model accounts for the fact that, even if water levels are higher in the Wadden Sea, wave set-up can still create a water level gradient that is directed towards the Wadden Sea. A comparison for all floodings shows (Figure A2a) a maximum offset of 0.14 m and an  $r^2$  value of 0.95 with no bias.

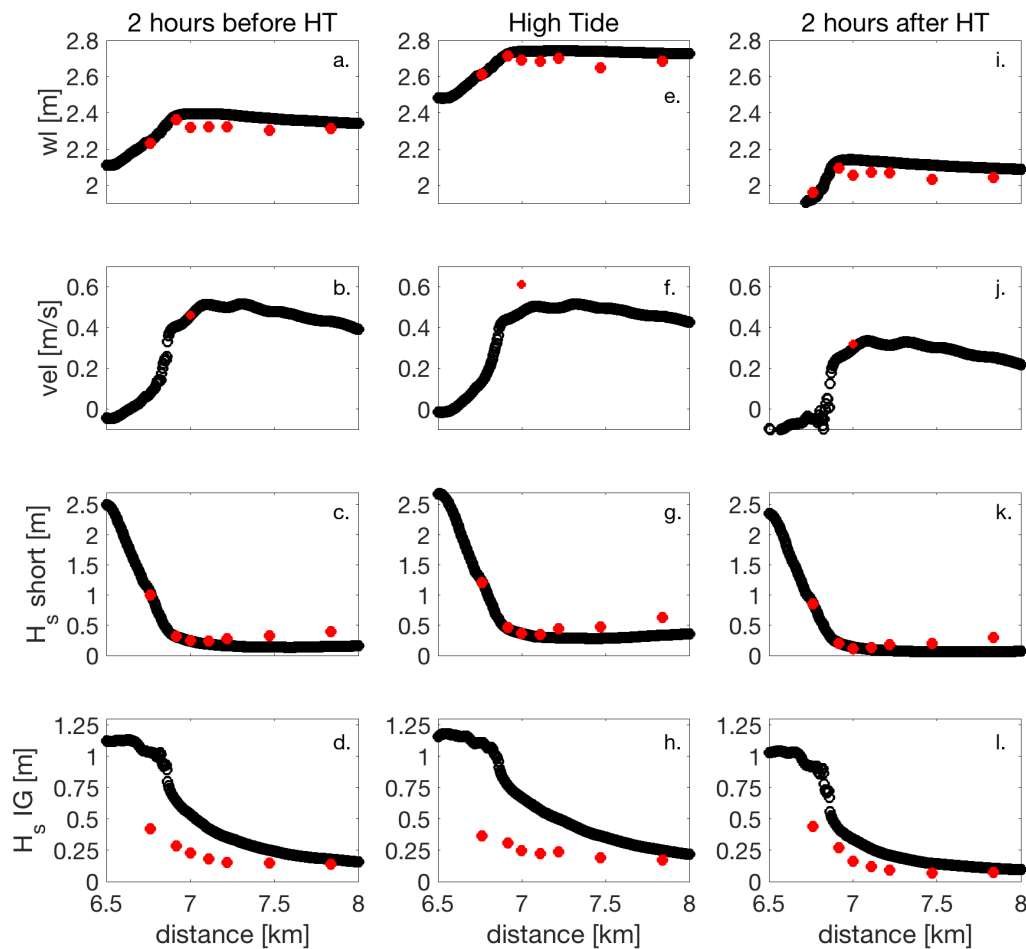


**Figure A1.** Observed (red) and modeled (black) water levels (wl, a, e, and i), cross-shore velocities (vel, b, f, and j), short (c, g, and k) and IG (d, h, and l) significant wave heights ( $H_s$ ) from 2 h before to 2 h after high tide (HT) for flooding 1. The North Sea is to the left and the Wadden Sea to the right in this graph.

Predicted mean velocities show satisfactory agreement with the observations for flooding 1 (Figure A1), albeit they were underestimated during high tide by  $\sim 0.13$  m/s. Generally, the model underestimated higher mean flow velocities ( $>0.3$  m/s) up to 0.3 m/s (Figure A2b), either because the implemented water levels were not correct, or the model was misrepresenting some local or physical processes.

While predicted short-wave heights showed good agreement with the observations for the first 3–4 locations on the North Sea side (Figure A1c,g,k), they were increasingly underpredicted towards the Wadden Sea, which can be seen in Figure A2c for all floodings (with a maximum underestimation of  $\sim 0.29$  m). This was expected since waves generated in the Wadden Sea were observed to propagate seawards [8], which was ignored in the model implementation. Infragravity-wave heights, on the other hand, were consistently overestimated (Figures A1d,h,l and A2d), especially on the North Sea, side by roughly a factor of 2. This was caused by our choice of using a 1D model (see Section 2.1) and hence the neglect of wave spreading on IG waves. The overestimation of IG waves might also have contributed to the underestimation of mean flow velocities by increasing the bottom friction which slows the flow.

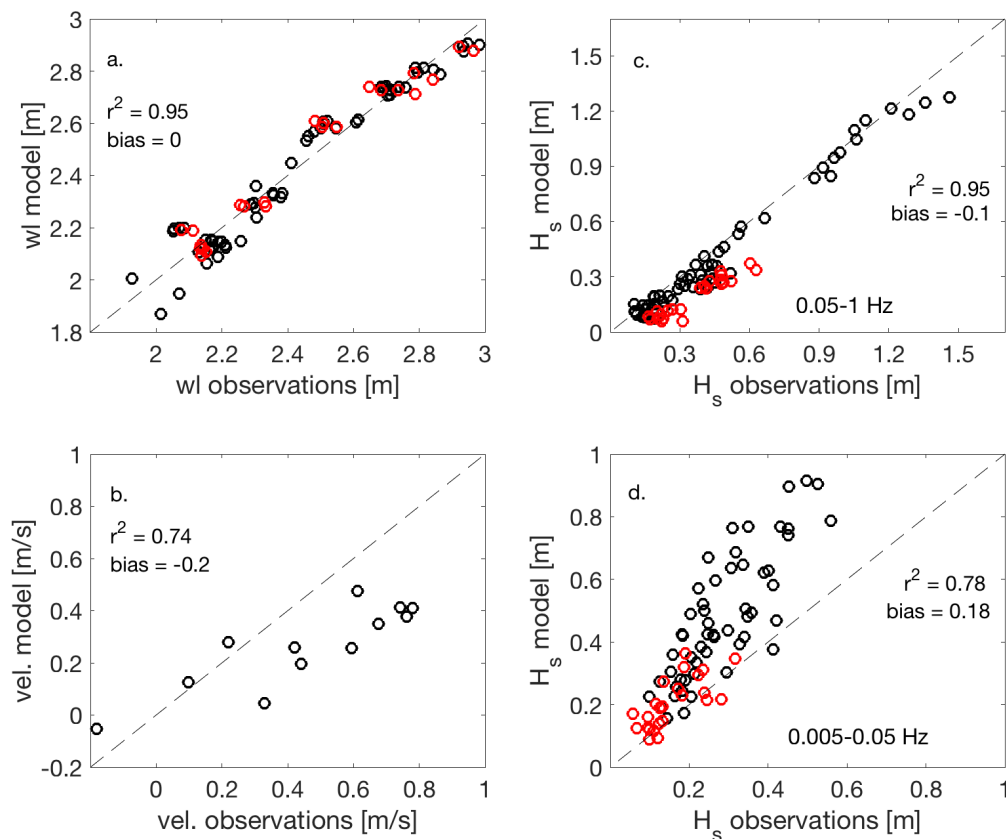


**Figure A2.** Observed and modeled water levels (wl, **a**), cross-shore velocities (vel, **b**), and short- (**c**) and IG (**d**) significant wave heights ( $H_s$ ) for all 4 floodings from 1 h before until 1 h after high tide (hourly output). The red circles indicate measurements at P5 and P6, the instruments closest to the Wadden Sea.

In order to compare the wave shape, short-wave asymmetries and skewness were limited to the frequency range 0.05–0.3 Hz to exclude waves propagating seaward from the Wadden Sea [8] and locally generated wind waves. Predictions of wave asymmetry and skewness show that the model is able of capturing the general trends (Figure A3). While short-wave asymmetry was overpredicted by far (Figure A4), the locations of the highest asymmetry (between  $x = 6.9$  and  $x = 7.2$  km, Figure A3a,c,e) were captured, as well as the changes during the tidal stages with the lowest asymmetries during high tide and the highest at two hours after high tide. Short-wave skewness was captured well.

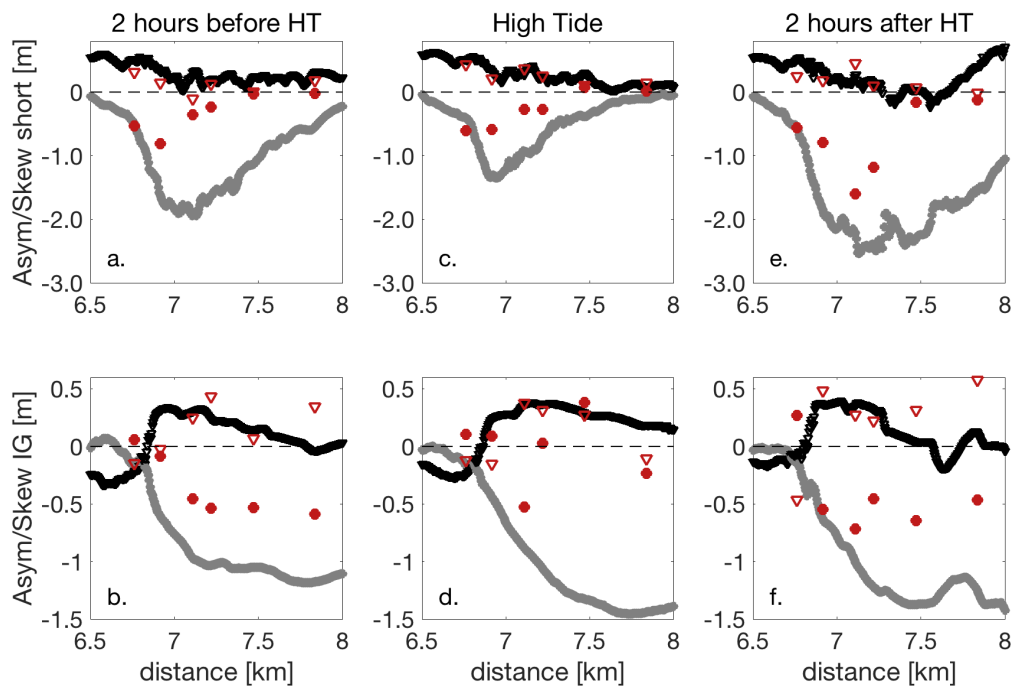


**Figure A3.** Observed wave asymmetry (red dots) and skewness (red triangles) compared to modeled wave asymmetry (gray) and skewness (black) from 2 h before until 2 h after high tide (HT) for flooding 1. The North Sea is to the left and the Wadden Sea to the right in this graph.

IG wave asymmetry was, as for short waves, highly overpredicted (Figure A3b,d,f), which was possibly caused by the overprediction of IG wave heights. However, the slight continuous increase two hours before high tide (Figure A3b), as well as the decrease at the location closest to the basin (Figure A3f) were captured by the model. The observed negative IG wave skewness and the following increases and decreases in positive IG skewness on the island were captured well for flooding 1, with the exception of the location closest to the Wadden Sea for which the observed skewness suddenly increased again. However, the  $r^2$  value (0.075) shows little relationship between observed and modeled IG skewness (Figure A4d), even though we only considered the first three locations to avoid any interference from the Wadden Sea processes. This is probably caused by a later (more landward) transformation of the observed IG skewness from negative to positive (see, e.g., Figure A3b,d), in addition to local variations in observed IG skewness (see Figure A3a, the third location from the North Sea). Generally, observed wave asymmetry and skewness fluctuated strongly from one instrument location to the other, especially for IG asymmetry and skewness (Figure A3b,d,f).

SWASH was able to reproduce the varying water levels including wave set-up and increased water levels in the Wadden Sea, short wave heights and cross-shore velocities reasonably well over a wide range of observed hydrodynamic conditions and tidal stages. While IG wave heights and wave asymmetries were largely overpredicted, SWASH reproduced the general trends seen in the observations, including the negative skewness. This suggests that the SWASH model is suited for an exploratory investigation of wave and current related sediment transport processes when focusing on the changes of each process (current-, IG- and short wave related suspension and transport), under varying island geometries and hydrodynamic forcing.

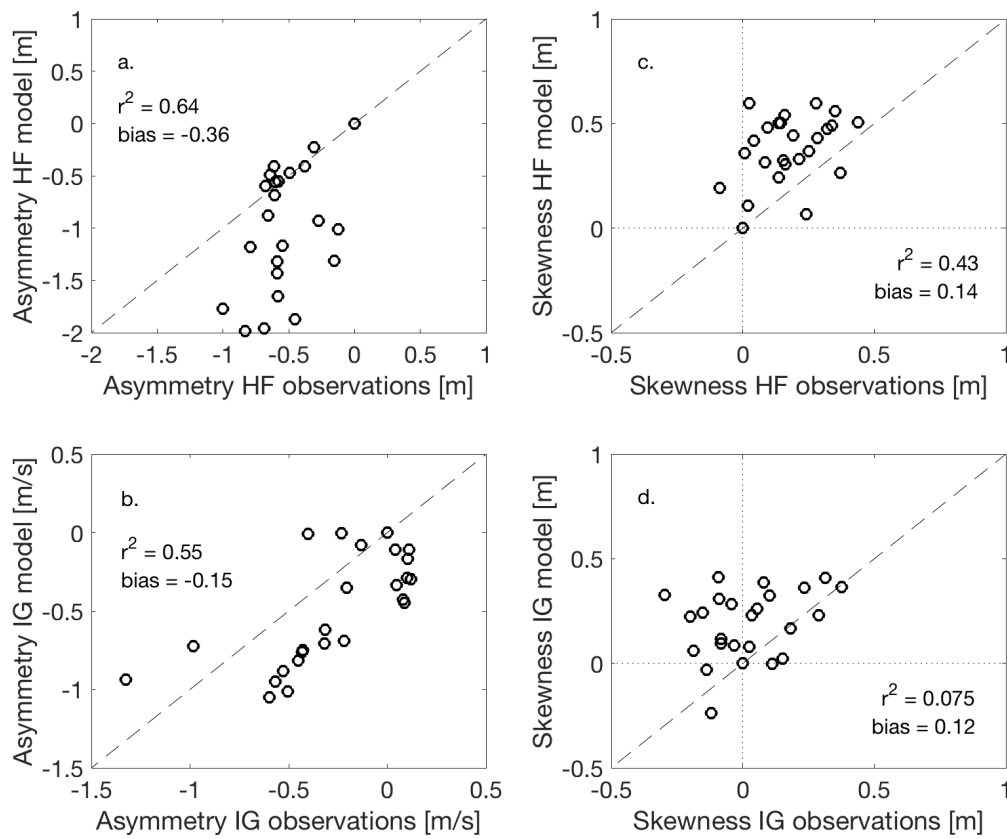


**Figure A4.** Observed and modeled short (HF, **a** and **c**) and infragravity (IG, **b** and **d**) wave asymmetry (**a** and **b**) and skewness (**c** and **d**) for all four floodings from 1 h before until 1 h after high tide (hourly output) for the first three instrument locations on the North Sea side.

## References

1. Donnelly, C.; Kraus, N.; Larson, M. State of Knowledge on Measurement and Modeling of Coastal Overwash. *J. Coast. Res.* **2006**, *22*, 965–991. [[CrossRef](#)]
2. Sallenger, A.H., Jr. Storm impact scale for barrier islands. *J. Coast. Res.* **2000**, *16*, 890–895. [[CrossRef](#)]
3. Safak, I.; Warner, J.C.; List, J.H. Barrier island breach evolution: Alongshore transport and bay-ocean pressure gradient interactions. *J. Geophys. Res. Oceans* **2016**, *121*, 8720–8730. [[CrossRef](#)]
4. Durán, R.; Guillén, J.; Ruiz, A.; Jiménez, J.A.; Sagristà, E. Morphological changes, beach inundation and overwash caused by an extreme storm on a low-lying embayed beach bounded by a dune system (NW Mediterranean). *Geomorphology* **2016**, *274*, 129–142. [[CrossRef](#)]
5. Donnelly, C. Morphologic Change by Overwash: Establishing and Evaluating Predictors. *J. Coast. Res.* **2007**, *23*, 520–526.
6. Rosati, J.; Stone, G.W. Critical Width of Barrier Islands and Implications for Engineering Design. In Proceedings of the Sixth International Symposium on Coastal Engineering and Science of Coastal Sediment Process, New Orleans, LA, USA, 13–17 May 2007; pp. 1–14. [[CrossRef](#)]
7. Engelstad, A.; Ruessink, B.G.; Hoekstra, P.; van der Vegt, M. Sand Suspension and Transport During Inundation of a Dutch Barrier Island. *J. Geophys. Res. Earth Surf.* **2018**, *123*, 3292–3307. [[CrossRef](#)]
8. Engelstad, A.; Ruessink, B.; Wesselman, D.; Hoekstra, P.; Oost, A.; van der Vegt, M. Observations of waves and currents during barrier island inundation. *J. Geophys. Res. Oceans* **2017**, *122*, 3152–3169. [[CrossRef](#)]
9. Sherwood, C.R.; Long, J.W.; Dickhudt, P.J.; Dalyander, P.S.; Thompson, D.M.; Plant, N.G. Inundation of a barrier island (Chandeleur Islands, Louisiana, USA) during a hurricane: Observed water-level gradients and modeled seaward sand transport. *J. Geophys. Res. Earth Surf.* **2014**, *119*, 1498–1515. [[CrossRef](#)]

10. Harter, C.; Figlus, J. Numerical modeling of the morphodynamic response of a low-lying barrier island beach and foredune system inundated during Hurricane Ike using XBeach and CSHORE. *Coast. Eng.* **2017**, *120*, 64–74. [[CrossRef](#)]
11. Hoekstra, P.; ten Haaf, M.; Buijs, P.; Oost, A.; Klein Breteler, R.; van der Giessen, K.; van der Vegt, M. Washover development on mixed-energy, mesotidal barrier island systems. *Coast. Dyn.* **2009**, *83*, 25–32. [[CrossRef](#)]
12. Wesselman, D.; Winter, R.; Engelstad, A.; McCall, R.; Dongeren, A.; Hoekstra, P.; Oost, A.; Vegt, M. The effect of tides and storms on the sediment transport across a Dutch barrier island. *Earth Surf. Process. Landf.* **2017**, *43*, 579–592. [[CrossRef](#)]
13. Van Dongeren, A.; Battjes, J.; Janssen, T.; Van Noorloos, J.; Steenhauer, K.; Steenbergen, G.; Reniers, A.J.H.M. Shoaling and shoreline dissipation of low-frequency waves. *J. Geophys. Res. Oceans* **2007**, *112*. [[CrossRef](#)]
14. De Bakker, A.T.M.; Tissier, M.F.S.; Ruessink, B.G. Shoreline dissipation of infragravity waves. *Cont. Shelf Res.* **2014**, *72*, 73–82. [[CrossRef](#)]
15. De Bakker, A.T.M.; Brinkkemper, J.A.; van der Steen, F.; Tissier, M.F.S.; Ruessink, B.G. Cross-shore sand transport by infragravity waves as a function of beach steepness. *J. Geophys. Res. Earth Surf.* **2016**, *121*, 1786–1799. [[CrossRef](#)]
16. Ruessink, B.G.; Kleinhans, M.G.; den Beukel, P.G.L. Observations of swash under highly dissipative conditions. *J. Geophys. Res. Oceans* **1998**, *103*, 3111–3118. [[CrossRef](#)]
17. Stockdon, H.F.; Holman, R.A.; Howd, P.A.; Sallenger, A.H. Empirical parameterization of setup, swash, and runup. *Coast. Eng.* **2006**, *53*, 573–588. [[CrossRef](#)]
18. de Bakker, A.T.M.; Tissier, M.F.S.; Ruessink, B.G. Beach steepness effects on nonlinear infragravity-wave interactions: A numerical study. *J. Geophys. Res. Oceans* **2015**, *121*, 554–570. [[CrossRef](#)]
19. Rosati, J.D.; Stone, G.W. Geomorphologic Evolution of Barrier Islands along the Northern U.S. Gulf of Mexico and Implications for Engineering Design in Barrier Restoration. *J. Coast. Res.* **2009**, *25*, 8–22. [[CrossRef](#)]
20. Schupp, C.A.; Winn, N.T.; Pearl, T.L.; Kumer, J.P.; Carruthers, T.J.; Zimmerman, C.S. Restoration of overwash processes creates piping plover (*Charadrius melodus*) habitat on a barrier island (Assateague Island, Maryland). *Estuar. Coast. Shelf Sci.* **2013**, *116*, 11–20. [[CrossRef](#)]
21. Zijlema, M.; Stelling, G.; Smit, P. SWASH: An operational public domain code for simulating wave fields and rapidly varied flows in coastal waters. *Coast. Eng.* **2011**, *58*, 992–1012. [[CrossRef](#)]
22. Rijnsdorp, D.P.; Smit, P.B.; Zijlema, M. Non-hydrostatic modelling of infragravity waves under laboratory conditions. *Coast. Eng.* **2014**, *85*, 30–42. [[CrossRef](#)]
23. Smit, P.; Janssen, T.; Holthuijsen, L.; Smith, J. Non-hydrostatic modeling of surf zone wave dynamics. *Coast. Eng.* **2014**, *83*, 36–48. [[CrossRef](#)]
24. Rijnsdorp, D.P.; Ruessink, G.; Zijlema, M. Infragravity-wave dynamics in a barred coastal region, a numerical study. *J. Geophys. Res. Oceans* **2015**, *120*, 4068–4089. [[CrossRef](#)]
25. Fiedler, J.W.; Smit, P.B.; Brodie, K.L.; McNinch, J.; Guza, R.T. Numerical modeling of wave runup on steep and mildly sloping natural beaches. *Coast. Eng.* **2018**, *131*, 106–113. [[CrossRef](#)]
26. Rijnsdorp, D.; Smit, P.; Zijlema, M. Non-hydrostatic modelling of infragravity waves using SWASH. *Coast. Eng. Proc.* **2012**, *1*, 27. [[CrossRef](#)]
27. Guza, R.T.; Feddersen, F. Effect of wave frequency and directional spread on shoreline runup. *Geophys. Res. Lett.* **2012**, *39*, L11607. [[CrossRef](#)]
28. Bagnold, R.A. An Approach to the Sediment Transport Problem from General Physics. *U.S. Geol. Surv. Prof. Pap.* **1966**, *422-I*. [[CrossRef](#)]
29. Bailard, J.A. An energetics total load sediment transport model for a plane sloping beach. *J. Geophys. Res. Oceans* **1981**, *86*, 10938–10954. [[CrossRef](#)]
30. Drake, T.G.; Calantoni, J. Discrete particle model for sheet flow sediment transport in the nearshore. *J. Geophys. Res. Oceans* **2001**, *106*, 19859–19868. [[CrossRef](#)]
31. Hoefel, F.; Elgar, S. Wave-induced sediment transport and sandbar migration. *Science* **2003**, *299*, 1885–1887. [[CrossRef](#)] [[PubMed](#)]
32. Smit, P.; Zijlema, M.; Stelling, G. Depth-induced wave breaking in a non-hydrostatic, near-shore wave model. *Coast. Eng.* **2013**, *76*, 1–16. [[CrossRef](#)]
33. Thornton, E.B.; Humiston, R.T.; Birkemeier, W. Bar/trough generation on a natural beach. *J. Geophys. Res. Oceans* **1996**, *101*, 12097–12110. [[CrossRef](#)]

34. Gallagher, E.L.; Elgar, S.; Guza, R. Observations of sand bar evolution on a natural beach. *J. Geophys. Res. Oceans* **1998**, *103*, 3203–3215. [[CrossRef](#)]
35. Ruessink, B.G.; Houwman, K.T.; Hoekstra, P. The systematic contribution of transporting mechanisms to the cross-shore sediment transport in water depths of 3 to 9 m. *Mar. Geol.* **1998**, *152*, 295–324. [[CrossRef](#)]
36. Janssen, T.T.; Battjes, J.A.; van Dongeren, A.R. Long waves induced by short-wave groups over a sloping bottom. *J. Geophys. Res. Oceans* **2003**, *108*, 3252. [[CrossRef](#)]
37. Tissier, M.; Bonneton, P.; Michallet, H.; Ruessink, B.G. Infragravity-wave modulation of short-wave celerity in the surf zone. *J. Geophys. Res. Oceans* **2015**, *120*, 6799–6814. [[CrossRef](#)]
38. Symonds, G.; Black, K.P.; Young, I.R. Wave-driven flow over shallow reefs. *J. Geophys. Res.* **1995**, *100*, 2639. [[CrossRef](#)]
39. Aagaard, T.; Greenwood, B.; Hughes, M. Sediment transport on dissipative, intermediate and reflective beaches. *Earth-Sci. Rev.* **2013**, *124*, 32–50. [[CrossRef](#)]
40. Butt, T.; Russell, P. Suspended sediment transport mechanisms in high-energy swash. *Mar. Geol.* **1999**, *161*, 361–375. [[CrossRef](#)]
41. Aagaard, T.; Greenwood, B. Suspended sediment transport and the role of infragravity waves in a barred surf zone. *Mar. Geol.* **1994**, *118*, 23–48. [[CrossRef](#)]
42. Goff, J.A.; Allison, M.A.; Gulick, S.P.S. Offshore transport of sediment during cyclonic storms: Hurricane Ike (2008), Texas Gulf Coast, USA. *Geology* **2010**, *38*, 351–354. [[CrossRef](#)]
43. Elgar, S.; Gallagher, E.L.; Guza, R.T. Nearshore sandbar migration. *J. Geophys. Res. Oceans* **2001**, *106*, 11623–11627. [[CrossRef](#)]
44. Ruessink, B.G.; van den Berg, T.J.J.; van Rijn, L.C. Modeling sediment transport beneath skewed asymmetric waves above a plane bed. *J. Geophys. Res. Oceans* **2009**, *114*, C11021. [[CrossRef](#)]
45. Brinkkemper, J.A.; Aagaard, T.; de Bakker, A.T.M.; Ruessink, B.G. Shortwave Sand Transport in the Shallow Surf Zone. *J. Geophys. Res. Earth Surf.* **2018**, *123*, 1145–1159. [[CrossRef](#)] [[PubMed](#)]
46. Grasso, F.; Michallet, H.; Barthelemy, E. Sediment transport associated with morphological beach changes forced by irregular asymmetric, skewed waves. *J. Geophys. Res. Oceans* **2011**, *116*. [[CrossRef](#)]
47. Ruessink, B.G.; Michallet, H.; Abreu, T.; Sancho, F.; Van der A, D.A.; Van der Werf, J.J.; Silva, P.A. Observations of velocities, sand concentrations, and fluxes under velocity-asymmetric oscillatory flows. *J. Geophys. Res. Oceans* **2011**, *116*, C03004. [[CrossRef](#)]



© 2019 by the authors. Licensee MDPI, Basel, Switzerland. This article is an open access article distributed under the terms and conditions of the Creative Commons Attribution (CC BY) license (<http://creativecommons.org/licenses/by/4.0/>).